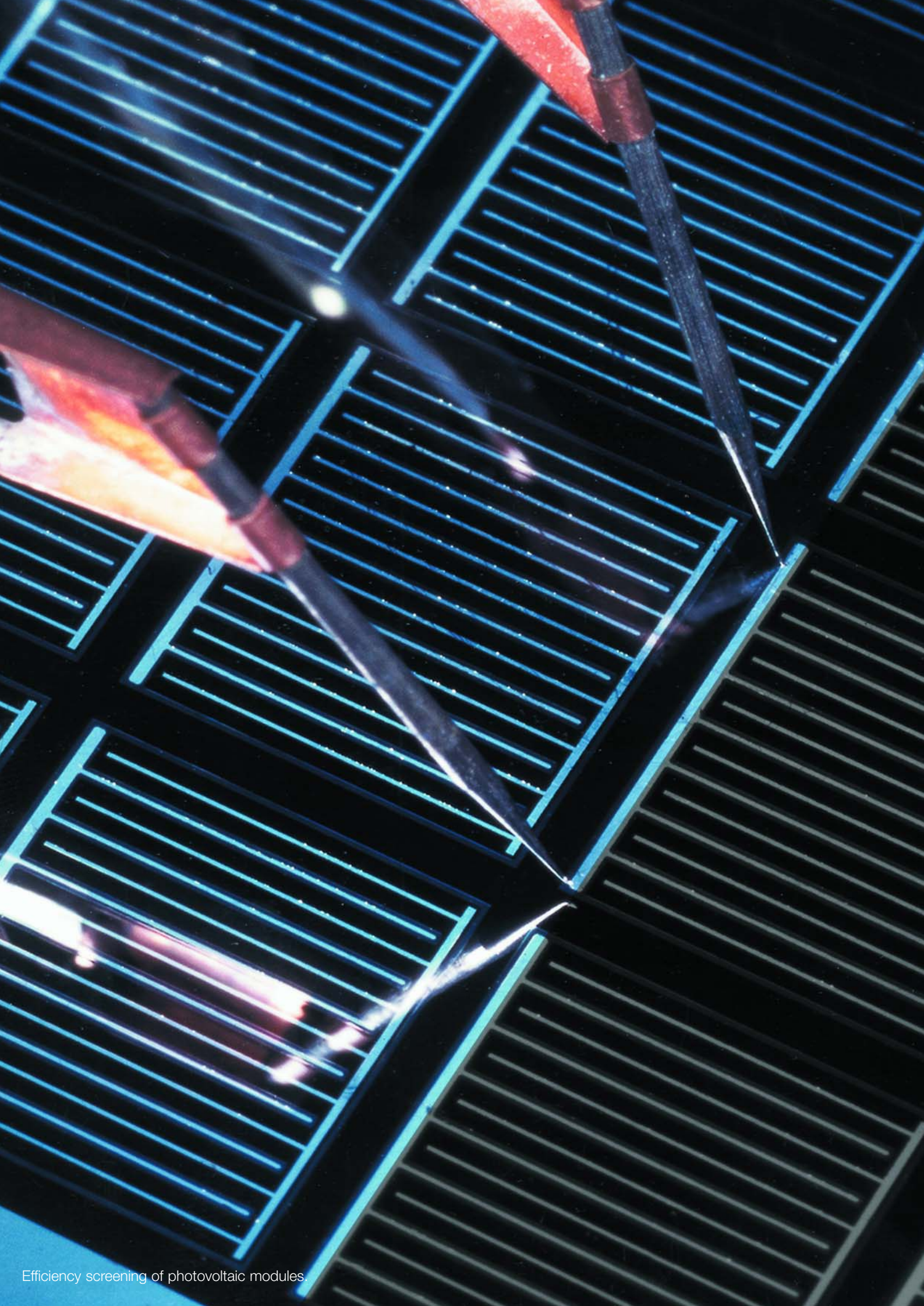


Annual Report 2003
Solar Energy Research



Efficiency screening of photovoltaic modules.

An aerial photograph of a solar farm, showing rows of solar panels stretching across a landscape. The panels are arranged in a grid pattern, with some rows appearing more prominent than others. The overall color palette is dark, with the solar panels appearing as a mix of dark blue and black, set against a lighter, hazy background. An orange rectangular bar is positioned at the top of the image, containing white text.

Scientific highlights Solar Energy Research 2003

SE1, Silicon Photovoltaics	S. 78
SE2, Heterogeneous Material Systems	S. 86
SE3, Technology	S. 104
SE4, Dynamics of Interfacial Reactions	S. 109
SE5, Solar Energetics	S. 114

Interface properties of a-Si:H/c-Si hetero-structures

K. Brendel, K. Kliefoth, L. Korte, A. Laades, D. Schaffarzik, A. Schoepke, R. Stangl, M. Schmidt

■ HMI, SE1

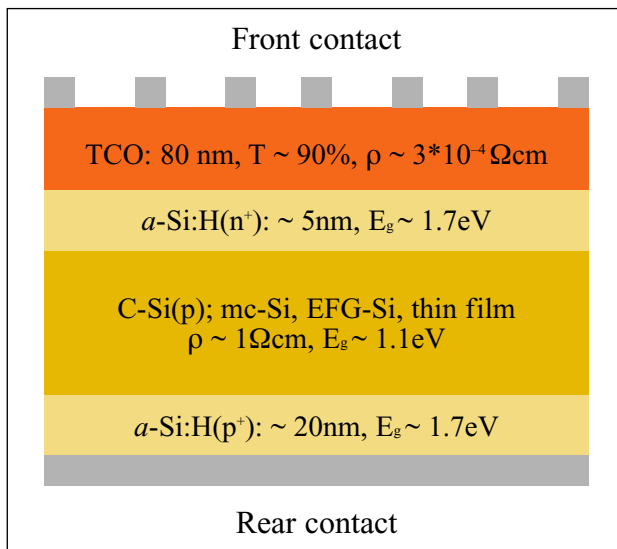


Fig. 1: Schema of a TCO/a-Si:H/c-Si hetero solar cell

The broad application of photovoltaic power systems requires a cost reduction. One way to reach this goal is the reduction of the thickness of the silicon absorber as an expensive part of such systems i.e. the application of thin low cost silicon wafers or silicon films on glass. Both need an adjusted technology for realising solar cells. The main requirement is to keep a temperature below 550°C during the hole manufacturing process. Simultaneously the loss mechanisms like recombination of the photo-carriers should be reduced in such cells for getting high efficiencies.

Silicon based heterojunction solar cells such as Transparent Conductive Oxide / amorphous – Silicon:H / crystalline Silicon are one example for such an high efficient solar cell structure which can be prepared by a complete low temperature process.

The efficiencies are dominated by the band offset for minority carrier injection from the c-Si(p) base, ΔE_C , the interface state density distribution at the a-Si:H/c-Si interface, $D_{it}(E)$, and the band bending in the c-Si absorber, $q\varphi_{s0}$, at the active hetero-transition, a-Si:H/c-Si.

The determination of these quantities is essential for developing a physically based technology. The optimum in the a-Si:H layer thickness amounts to about 5 nm. This minimises the absorption losses in the a-Si:H layer and it is possible to reach an optimum in band bending of the c-Si absorber. This very low film thickness corresponds to the emission depth of photoelectrons with kinetic energies below 10 eV. This allows to determine the work function, the position of the Fermi energy E_F and the distribution of occupied gap states $N(E)_{oc}$ of the a-Si:H layer by photoemission spectroscopy excited with energies between 4 eV and 7,5 eV. The precondition for determining $N(E)_{oc}$ is a nearly constant photoexcitation cross section and a constant density of states in the conduction band. Both are more or less fulfilled in a-Si:H.

The $N(E)_{oc}$ distributions are independent on the a-Si:H layer thickness. Only in the case of the 2.8 nm thick layer we found a deviation up to 0.4 eV above the a-Si:H valence band edge as indicated by the dotted line E_{Va-Si} in Fig. 3. This hints to a contribution of photoelectrons originating from the occupied valence band states of the underlying c-Si wafer which vanishes above the valence band edge of the c-Si,

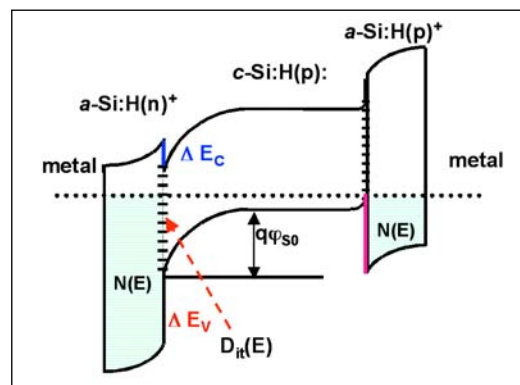


Fig. 2: Band schema of a TCO/a-Si:H/c-Si hetero solar cell. Interface state density $D_{it}(E)$, gap state density $N(E)$, conduction band offset ΔE_C , valence band offset ΔE_V and band bending $q\varphi_{s0}$ are indicated.

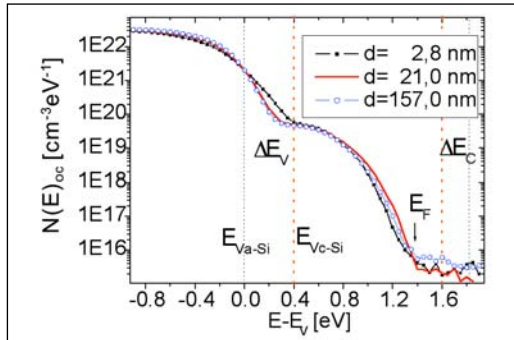


Fig. 3: $N_{oc}(E)$ of slightly n-doped a-Si:H of different film thickness prepared by PECVD on c-Si(p), (111), $75\Omega\text{cm}$). The data result from constant final state yield measurements, the chosen final state energy amounts to 200 meV. Excitation energy range $h\nu = 4.7$ eV. The arrow indicates the Fermi level position ($E_F - E_{Va-Si} = 1.33$ eV) and the dotted lines indicate the position of the band edges of c-Si and a-Si:H, respectively.

marked by the dotted line E_{Vc-Si} in Fig. 3. The analysis gives a valence band offset ΔE_V of 400 meV. Furthermore, the exponentially distributed valence band tail states and the deep dangling bond states at about 700 meV are clearly seen in Fig. 3.

The missing quantities like the c-Si band bending and the a-Si:H/c-Si interface state density can be determined by applying the surface photovoltage, SPV, method. In order to determine the band bending, $q\phi_{SO}$, or the interface state density, D_{it} , we use an artificial MIS structure, where the metal electrode consists of a TCO layer and the insulator constitutes of a mica foil. Excess charge carriers were generated in the c-Si by a light pulse of $\lambda = 910$ nm wavelength and 10–160 ns pulse length. This leads to a flattening of the band bending i.e. a change of the surface space charge. This change of the surface charge can be read out by a capacitively coupled high speed oscilloscope. The obtained quantity represents the photovoltage, U_{ph} , modified by the Dember-voltage which results from the mobility difference of electrons and holes.

Applying an additional external voltage U_{field} we are able to change the band bending by a field effect like in a MIS transistor. Thus, we can measure the c-Si band bending via the dependence of the photovoltage on the applied external voltage, $U_{ph} = f(U_{field})$. The charge components of such an MIS structure are divided into the charge located in the interface states, in the space charge of c-Si and in the charge

on the metal electrode. All in all we have charge neutrality, this is true also for different applied external voltages. With this method, the thin a-Si:H layer has to be treated like an insulator without change of the trapped charge during the whole measurement. This is only fulfilled at deep temperatures because the charge transfer processes between c-Si and a-Si:H are assisted by phonons which can be frozen and hence the a-Si:H(i) layer can be treated like an insulator.

The $D_{it}(E)$ spectra in Fig. 4 indicate an excellent passivation of the c-Si surface, better or comparable to the passivation by thermally grown SiO_2 or Si_3N_4 .

Further progress for SPV investigation by wavelength and intensity dependent measurements is in preparation.

Using the analytical methods for optimisation of the preparation steps, we are able to prepare hetero structure solar cells on flat p-type c-Si wafers with 17% efficiency and with about 14% on EFG silicon material.

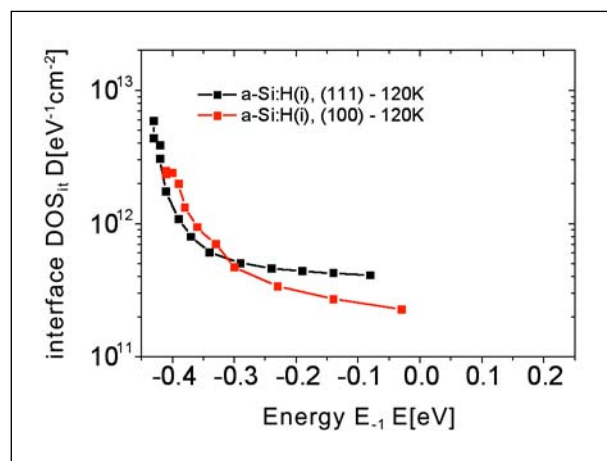


Fig. 4: $D_{it}(E)$ of the a-Si:H(i)/c-Si interface for [100] and [111] oriented Si surfaces. The a-Si:H layer thickness amounts to 20 nm.

M. Schmidt, A. Schöpke, O. Milch, Th. Lussky, W. Fuhs, Mat. Res. Soc. Symp. Proc. Vol. 762 (2003) A19.11.1

The nature of dangling bond recombination in silicon

C. Böhme and K. Lips

■ HMI, SE1

For thin-film silicon and silicon interfaces, unpaired silicon valence electrons, so called dangling bonds (db), are known to influence recombination rates significantly. In spite of this insight, the microscopic mechanisms associated with db recombination have remained unknown in the past.

Traditional ways to investigate recombination at db centers microscopically such as the continuous wave electrically or optically detected magnetic resonance (EDMR or ODMR) can not provide quantitative information such as recombination probabilities or capture cross sections nor can they distinguish qualitatively different electronic mechanisms which occur at the same defects. Other, non-magnetic resonance based defect spectroscopy methods such as capacitance voltage or deep level transient spectroscopy lack the microscopic sensitivity to distinguishable defects.

Because of this, coherent spin resonance based methods have been developed and improved at the Hahn-Meitner Institute Berlin in recent years [1, 2]. These methods, the pulsed (p) EDMR and pODMR have now been applied to different silicon thin-film materials and silicon related interfaces that are relevant for new solar cell concepts. The studies are to elaborate the qualitative nature of recombination mechanisms at db states and to clarify which of these mechanisms dominate net recombination rates. As an example, the results for hydrogenated microcrystalline silicon ($\mu\text{c-Si:H}$) are shown here. In the past, much speculation existed whether charge carriers in this material recombine at dangling bonds from trap states in band tails by distant-pair tunneling or whether they are directly captured from delocalized states. Due to the different nature of these mechanisms with regard to the coupling between defect and charge carrier or the influence of disorder, different pEDMR signatures can be expected for the two channels.

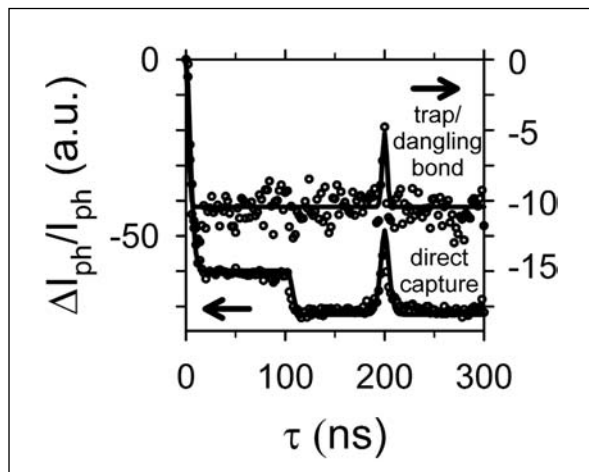


Fig. 1: PEDMR signal at db states of $\mu\text{c-Si:H}$ at $T = 10\text{ K}$ in case of direct capture and distant-pair-tunneling. The solid lines are theoretical predictions.

Figure 1 illustrates the photocurrent response of $\mu\text{c-Si:H}$ during such a short coherent electron-spin resonant (ESR) excitation of db states. The measurement was carried out as a "recombination echo" experiment where a 180° phase change of the microwave is introduced at $\tau_{180} = 100$ ns. Since the measurement is carried out at different times after the spin ensemble starts to relax back towards its steady state, the different recombination mechanisms can be identified due to their different recombination dynamics. The measurements show that two clearly distinguishable processes are present: Firstly, a strong step-like transient with a clear echo signature at $2\tau_{180} = 200$ ns. One can describe this observation with the predictions for recombination out of strongly coupled pair states [2] as expected for a direct capture process. Opposite to this observation, a second signature with reduced intensity is also found. This second signal does not exhibit the step-like dephasing at τ_{180} and the echo is much more narrow. This observation is indicative of recombination of weakly coupled charge carrier pairs with highly disordered local fields as it is known to exist for distant-pair tunneling. A detailed review of the nature of the different recombination channels at db centers of $\mu\text{c-Si:H}$ is outlined in Ref. [3].

Beside db centers in $\mu\text{c-Si:H}$, pEDMR and pODMR have been applied to db located at the crystalline silicon / silicon dioxide interfaces (so called P_b centers) as well as to the investigation of db and band tail recombination in amorphous silicon. Even though these different materials vary greatly with regard to their morphological and defect structures, conductivity mechanisms, band gap etc., the underlying mechanisms for charge carrier recombination appear to be of similar qualitative nature. The dominant recombination process at db centers in $\mu\text{c-Si:H}$ and at the crystalline silicon interface appears to be a direct capture process of electrons from the conduction band via charged excited intermediate states, so called db^* (Pb^* in the case of the interface): When electrons undergo transitions from a delocalized or weakly localized conduction band or band tail state, they localize first in these charged excited intermediate pair states, before they undergo an energy transition into the charged ground state. Thus, recombination at the silicon db seems to be less influenced by the respective microscopic environment of a given db and instead is determined by its own nature (size, wave function) which is known to be quite similar in different systems containing silicon db states.

-
- [1] C. Boehme, K. Lips:
Phys. Rev. Lett., **91** (24), 246603 (2003)
 - [2] C. Boehme, K. Lips:
Phys. Rev. B, **68** (24), 245105 (2003)
 - [3] C. Boehme, K. Lips:
phys. stat. sol. (c) **1** (5), 1255-1274 (2004)

Hydrogen in ZnO

N. H. Nickel, K. Brendel

■ HMI, SE1

In the past ZnO has been attracted a great deal of interest because of its optical and electrical properties for applications such as UV light emitting diodes and lasers. However, a major drawback of ZnO is the fact that it almost always shows *n*-type conductivity. Traditionally, the *n*-type conductivity has been attributed to the presence of native defects [1]. Recently, based on first-principles calculations a new source responsible for the observed *n*-type conductivity has been suggested namely, hydrogen atoms that act as shallow donors [2]. This behavior of hydrogen is unexpected since in most semiconductors it acts as a compensating center counteracting the existing conductivity. Most recently, the theoretical prediction has been confirmed experimentally by electron paramagnetic resonance, electron nuclear double resonance, and Hall effect measurements. These measurements revealed the presence of two donors in undoped single crystal ZnO one of which was identified as a hydrogen shallow donor that occurs in a concentration of about $6 \times 10^{16} \text{cm}^{-3}$ [3].

The presence of hydrogen in *as-grown* state-of-the-art single crystal ZnO gives rise to an unexpected variety of six H-related local vibrational modes in the wave number range between 2800 cm^{-1} and 3150 cm^{-1} . The vibrational modes are assigned to antisymmetric and symmetric stretching modes of CH_X complexes with $X = 1, 2, 3$. Hence, the vibrational modes located at 2854, 2890, 2918, 2948, and 2988 cm^{-1} would be due to the stretching modes of C-H, symmetric stretching modes of C-H_3 , symmetric stretching modes of C-H_2 , antisymmetric stretching modes of C-H_3 , and antisymmetric stretching modes of C-H_2 , respectively. This assignment is supported by the observation that a significant concentration of hydrocarbons is detectable in effusion experiments.

It is not unusual that local vibrational modes in solids occur at frequencies several percent lower than in a free molecule. Thus, the local vibrational mode at 3096 cm^{-1} is tentatively assigned to N-H complexes, which is corroborated by effusion data [4]. After dehydrogenation of the ZnO crystals the local vibrational modes disappeared. This clearly demonstrates that the local vibrational modes between 2800 cm^{-1} to 3150 cm^{-1} are due to hydrogen related stretching vibrations.

From H effusion data the H density-of-states distribution (DOS) can be derived using the relation $N_H \approx \partial C_H / \partial \mu_H$, where C_H is the H concentration and μ_H is the hydrogen chemical potential [5, 6]. In Fig. 2 the H DOS for sputtered (a) and single crystal ZnO is plotted (b). The lowest H DOS is obtained for single crystal ZnO. Deconvolution shows that the spectrum is composed of six peaks with the most prominent feature at 0.86 eV. An increase of the H concentration results in a broadening of the H DOS. Interestingly, with increasing H up to 75 % of the H atoms are accommodated with binding energies larger than 1.0 eV.

The results clearly show that the presence of H in ZnO causes the formation of a variety of complexes in addition to acting as a shallow donor. Using Raman spectroscopy C-H_X and N-H complexes were detected. In addition, the H density-of-states distribution reveals a number of peaks that are not yet assigned to specific centers. However, the pronounced increase of N_H for binding energies larger than 1.0 eV with increasing H content suggests the formation of larger H clusters.

-
- [1] D. C. Look, J. W. Hemsky, and J. R. Sizemore, Phys. Rev. Lett. **82**, 2552 (1999).
 - [2] C. G. Van de Walle, Phys. Rev. Lett. **85**, 1012 (2000).
 - [3] D. M. Hofmann, et al., Phys. Rev. Lett. **88**, 045504 (2002).
 - [4] N. H. Nickel and K. Fleischer, Phys. Rev. Lett. **90**, 197402 (2003).
 - [5] W. B. Jackson et al., J. Non-Cryst. Sol. **227-230**, 143 (1998).
 - [6] N. H. Nickel and K. Brendel, Phys. Rev. B **68**, 193303 (2003).

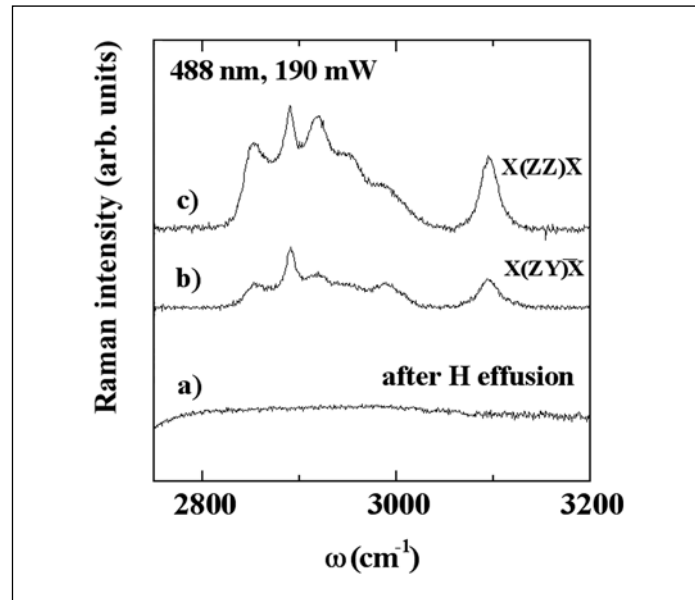


Fig. 1: Raman backscattering spectra of local vibrational modes in single crystal ZnO. Spectrum a) was measured after dehydrogenation of the sample. The spectra labeled b) and c) represent polarized Raman measurements on as-grown single crystal ZnO.

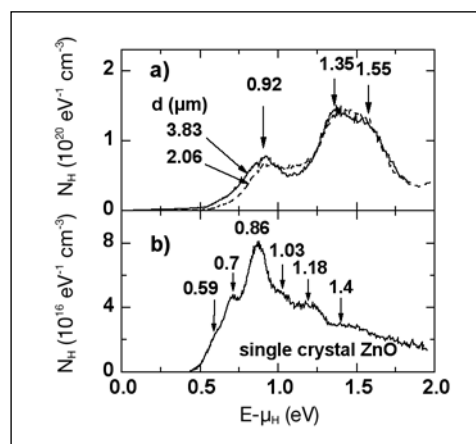


Fig. 2: H DOS in sputtered ZnO:Al (a) films and single crystal ZnO (b). The numbers along the spectra indicate the peak energies.

Electronic functionalisation of Si surfaces by thin organic layers

J. Rappich
 ■ HMI, SE1

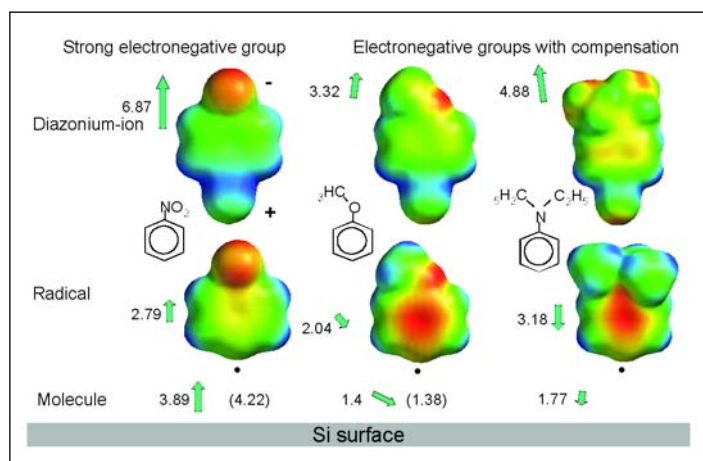


Fig. 1: Changes of the dipole strength and orientation of some organic molecules in different states (ion, radical and molecule) as calculated by DFT method (dipole strength in units of Debye, values in parenthesis are taken from literature; orientation is denoted by the arrow).

Organic materials (thin layers and polymers) become more and more important as reflected by recently developed thin film transistors, light emitting diodes (LED), and thin film solar cells, which are based on a mixture of organic polymers with C60. The great amount of possible combinations of organic groups makes them also of interest to build up especially designed buffer-layers on Si (or even on other semiconductors) to serve the following purposes:

1. Passivation of the interface to reduce recombination losses during current flow.
2. Change in band bending by surface dipoles, which induce a fixed electrical charge formed by electron donor or acceptor groups, i.e. $-\text{CH}_3$ or $-\text{NO}_2$.
3. Change in work function (i.e. band offset) of hetero structures on Si as a result of the surface dipole.
4. Formation of hydrophilic or hydrophobic surface condition for a better sticking of a deposited layer.

In order to form such organic layers on silicon we used electrochemical grafting of organic molecules on hydrogenated Si surfaces in aqueous electrolytes. The organic molecules consist of an aryl compound with a diazonium group (^+N -aryl-G) where G is a variable electron donor or acceptor group, which defines the orientation and strength of the dipole moment (Fig. 1).

The deposition process is performed at room temperature by applying a cathodic current to the Si electrode (electron injection into the electrolyte). Cathodic polarisation prevents the Si surface against oxidation.

In-situ photoluminescence and photovoltage, ex-situ Kelvin probe (CPD), and TEM measurements have been used to characterise changes in surface recombination velocity, band bending, work function, and interface structure. The in-situ measured change in photovoltage after and before grafting of organic molecules on the hydrogenated Si surface (ΔU_{PV}), which is identical to the change in band bending, and the ex-situ obtained work function (CPD values) are plotted in Fig. 2 against the effective dipole moment of the organic molecule perpendicular to the Si(111) surface.

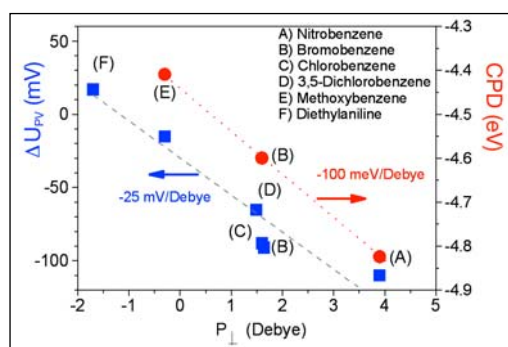


Fig. 2: Changes in band bending (ΔU_{PV}) and work function (CPD) as a function of effective dipole perpendicular to the Si(111) surface, (A to F) with the strongest and weakest electron acceptor group.

The grafting of thin layer of a diazonium compound (e.g. diethylaniline and nitrobenzene) on atomically flat p -Si(111):H surfaces induces a change of the band bending of about +20 and -110 meV, respectively. The in-situ measured band bending changes by about -25 mV/Debye. This change is lower than that measured ex-situ by SPV, indicating the screening of the effective dipole of the organic molecule by the surrounded water dipoles. In addition, the work function shifts also with the dipole moment by about -100 meV/Debye. The amount of nonradiative surface defects (N_s) increases only slightly by a factor of about 3 with respect to the perfect hydrogenated Si surface ($N_s < 10^{11} \text{cm}^{-2}$).

The electrochemical deposition of organic layers on flat n -Si(111) surface leads to the formation of a well ordered interface as observed by high resolution transmission electron microscopy images (HRTEM), see Fig. 3. Therefore, the changes in band bending is highest on flat surfaces and is less pronounced when a rough Si surface (the dipoles are no longer regularly ordered at the surface) or even a thin oxide covered Si surface is used for the deposition process [1–4].

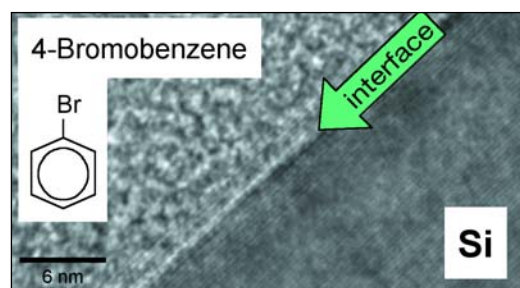


Fig. 3: HRTEM of an organic layer on n -Si(111), the arrow denotes the interface position.

Fig. 4 compares the N_{1s} NEXAFS spectra [5] obtained at flat n -Si(111) surfaces after electrochemical deposition of 4-nitrobenzene for 10 and 100 s. The broad NEXAFS spectrum after 10 s of deposition time is dominated by the σ^* resonance of nitrogen at about 405 eV. Besides the broad spectrum of the σ^* resonance, two narrow peaks of the π^* resonance appear around 393 and 397 eV after 100 s of deposition time. The stronger resonance at 397 eV can be seen as a shoulder also after the deposition time of 10 s.

The broad peak of the σ^* resonance can be assigned to nitrogen bounded to carbon and/or oxygen. The appearance of the π^* resonance is equivalent to the formation of $N=N$ bonds which can arise during electrochemical polymerization of nitrobenzene.

These results show that thin organic layers can be electrochemically deposited onto Si surfaces. These organic layers are able to passivate the interface and to influence the band bending and work function of Si which is induced by charge transfer via the formed Si-C bond. The change in work function was about 100 meV per Debye. Too long electrodeposition should be avoided due to polymerization of the diazonium compound.

The next step will be the formation of electrical contacts upon these layers and to investigate these contacts in more details, even in use as hetero structure solar cells.

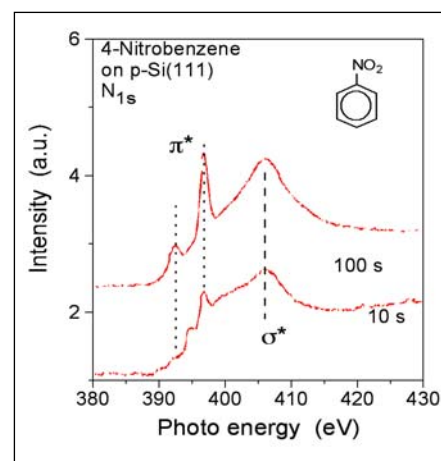


Fig. 4: N_{1s} NEXAFS spectra obtained at flat n -Si(111) surfaces after electrochemical deposition of 4-nitrobenzene for 10 and 100 s.

- [1] P. Hartig, J. Rappich, and Th. Dittrich, *Engineering of Si surfaces by electrochemical grafting of p-nitrobenzene molecules*, Appl. Phys. Lett., **80**(1), 67–69 (2002)
- [2] P. Hartig, Th. Dittrich, and J. Rappich, *Surface dipole formation and nonradiative recombination at p-Si(111) surfaces during electrochemical deposition of organic layers*, J. Electroanal. Chem., **524–525**, 120–126 (2002)
- [3] P. Hartig, Th. Dittrich, J. Rappich, Patentanmeldung 101 30 801.9; *Verfahren zur Funktionalisierung und Passivierung der Oberfläche von Silizium-Wafern durch elektrochemische Abscheidung dünner organischer Schichten*,
- [4] P. Hartig, J. Rappich, M. Portwich, R. Volkmer-Engert, Patentanmeldung 103 34 096.3; *Verfahren zum Herstellen einer Anordnung mit mehreren Schichten auf Basis eines Halbleitersubstrates und Mehrschichtanordnung*
- [5] D.R. Batchelor, P.R. Bressler, P. Hartig, J. Rappich, Th. Dittrich, *NEXAFS and photoemission investigation of electrochemically deposited organic layers on p-Si(111)*; Bessy Annual Report 2001.

Do we really need another photoluminescence study on CuInSe_2 ?

S. Siebentritt, N. Rega, J. Albert, A. Zajogin

■ HMI, SE2

They have been performed since the seventies! Yes, we do. Here is the problem: good solar cells with efficiencies up to 19.2 % can be made from Cu(In,Ga)Se_2 with a low content in Ga, i.e. with low band gaps. To prepare thin film tandem solar cells we need CuGaSe_2 solar cells with an efficiency of at least 15 %. Nobody in the world makes CuGaSe_2 solar cells with an efficiency of even 10 %. The question is, is there a fundamental difference between the absorber materials CuInSe_2 and CuGaSe_2 ? Our approach is to investigate the defect spectra of these materials by photoluminescence (PL). Our previous study on CuGaSe_2 has already shown that the doping defects are represented by two acceptors and a shallow donor, that their relative concentrations depend on the composition. And that due to the high degree of compensation in Cu-poor material the observed emissions at lower energies are not due to new defects but due to potential fluctuations.

Can't we just compare this result to the literature data for CuInSe_2 and find out, if there are differences in the defect spectra? No, we can't. First of all, literature data is contradicting, no consensus has been found yet on the defects in CIS. Then, the defect spectrum is dependent on the composition. If this information is not given it is difficult to compare the spectra. And finally, to exclude differences due to different preparation methods, only spectra from CuInSe_2 and CuGaSe_2 prepared by the same method can be directly compared. There are very few studies that take all this into account. They do not agree with each other, nor with our results on CuGaSe_2 (although their measurement results can be explained within the frame of our model). Generally they find one acceptor less in CuGaSe_2 than in CuInSe_2 .

In addition, the few studies on the luminescence of Cu(In,Ga)Se_2 with varying Ga content have not obtained any information on defects, they just observe that the spectra shift with the band gap.

This is where our PL investigations come in. We have CuInSe_2 , Cu(In,Ga)Se_2 and CuGaSe_2 prepared by the same MOVPE process. We have epitaxial films without the influence of grain boundaries. We have already a detailed study on the PL of CuGaSe_2 .

Therefore a composition, temperature and intensity dependent study of the PL of CuInSe_2 was performed. The figure compares the PL spectra of CuGaSe_2 and CuInSe_2 obtained for different $[\text{Cu}]/[\text{In}]$ or $[\text{Cu}]/[\text{Ga}]$ ratios. The shape of the spectra and their composition dependence look very similar. A detailed temperature and intensity dependent study of the CuInSe_2 shows that the defect spectrum of CuInSe_2 , as of CuGaSe_2 consists of two acceptors and a shallow donor. They are somewhat shallower than those in CuGaSe_2 : at 40 and 60 meV from the valence band edge and about 10 meV from the conduction band edge.

The next step is to investigate the PL spectra of $\text{Cu}(\text{In,Ga})\text{Se}_2$ for varying Ga content. Since for Ga ratios around 80 % the $\text{Cu}(\text{In,Ga})\text{Se}_2$ luminescence overlaps with the luminescence from the GaAs substrate, the PL measurements are supplemented by spatially resolved cathodoluminescence spectra. We find for the first time excitonic luminescence for $\text{Cu}(\text{In,Ga})\text{Se}_2$ with a Ga ratio below 30 % or above 70 %. The defect related luminescence broadens considerably for a Ga ratio between 30 and 70 % due to disorder effects between Ga and In sites. Defect energies are extracted from temperature dependent measurements, they are compatible with a linear variation between the defect energies in CuInSe_2 and CuGaSe_2 .

Therefore it is concluded that no fundamental difference concerning the defect spectra exists within the $\text{Cu}(\text{In,Ga})\text{Se}_2$ system. Thus it is not due to the defect spectrum that solar cells made of CuGaSe_2 absorbers show lower efficiencies and the chance for their improvement exists.

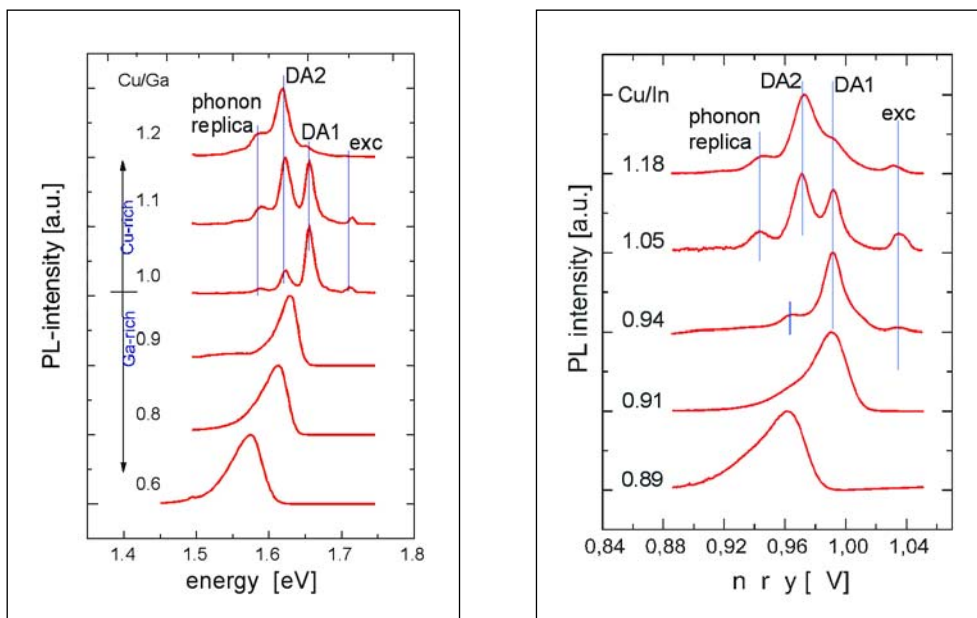


Fig. 1: PL spectra of CuGaSe_2 (left) and CuInSe_2 (right) as a function of the $[\text{Cu}]/[\text{III}]$ ratio

A novel approach to chalcopyrite-based heterojunctions

R. Klenk, Th. Glatzel, A. Grimm, H. Steigert, I. Lauermann

■ HMI, SE2

A typical chalcopyrite-based solar module consists of five thin films deposited sequentially onto a glass substrate: a metallic back contact (molybdenum), absorber (chalcopyrite), buffer layer (CdS), window layer 1 (ZnO) and window layer 2 (ZnO:Al). Depending on the manufacturing technology additional films are added, acting as diffusion blockers or sodium source. Optimisation of production cost and yield demands a reduction in the number of processes.

Elimination of the buffer layer appears particularly attractive because its preparation requires the handling of cadmium-containing raw materials and waste. Furthermore, this film is the only one to be deposited by wet chemistry which prevents completely dry in-line manufacturing of the module.

Previous models ascribed the importance of the CdS buffer layer to the matching of lattice constants and to the prevention of sputter damage during window layer deposition. However, numerical calculations show that a very high density of defects at the heterointerface can be tolerated if certain conditions are met [1]. They include the alignment of the conduction band and the net electrical charge within the defect distribution (Fig. 1). If the buffer layer is omitted, the window layer 1 defines the pn-junction (hetero interface) and has to be modified to meet the cited requirements. Literature data [2] and theoretical considerations indicated a promising approach in which ZnO is replaced by (Zn,Mg)O. Accordingly, the goal has been to reach high efficiency with a modified solar cell where the buffer layer was omitted and the ZnO replaced by (Zn,Mg)O.

Results of structural and optical characterisation show that single phase (Zn,Mg)O films with Mg/Zn ratios of 0.15 and 0.3 can be prepared by sputtering from a single mixed target allowing straightforward integration into existing production lines. The solar cell efficiency without buffer layer increased from 6 % (ZnO) to values around 10 % for Zn_{0.85}Mg_{0.15}O and

reached 12.5 % after optimisation with Zn_{0.7}Mg_{0.3}O, the latter value being comparable to the efficiency of reference cells with buffer layer. Current transport analysis indicates that recombination at the heterointerface does indeed not contribute significantly to the diode current in optimised cells with or without buffer layer.

Formation of the direct chalcopyrite/window interface has been investigated by synchrotron-excited photo electron spectroscopy. Oxidation of the chalcopyrite surface is detected during the initial stage of window layer growth (Fig. 2). Contrary to our initial assumption that the more stable MgO releases less oxygen, thereby preserving the crucial positive interface charge, no significant differences between ZnO and (Zn,Mg)O could be found so far with respect to chalcopyrite oxidation.

Reproducibility of cell results was good as long as a certain type of absorber from the Shell-Solar pilot production had been used (Cu(In,Ga)(Se,S)₂, CIGSSe). The properties of the chalcopyrite absorber surface are more critical in the novel structure. Hence, future work shall focus on making the structure applicable to a wider range of absorbers, in particular wide-gap chalcopyrites. Understanding the interface formation and relating it to the electronic models is considered essential for achieving this goal.

[1] R. Klenk, *Thin Solid Films* **387**, 135–140 (2001).

[2] T.Minemoto, T.Negami, S.Nishiwaki, H.Takakura, Y.Hamakawa, *Thin Solid Films* **372**, 173–176 (2000).

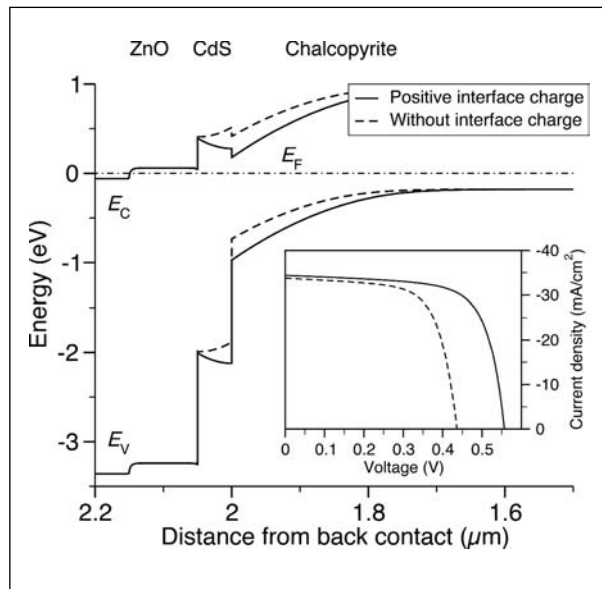


Fig. 1: Calculated band diagrams of chalcopyrite-based heterojunctions with positive and without any interface charge. The inset shows the corresponding jV characteristics. Note the loss in device performance in the absence of positive interface charge.

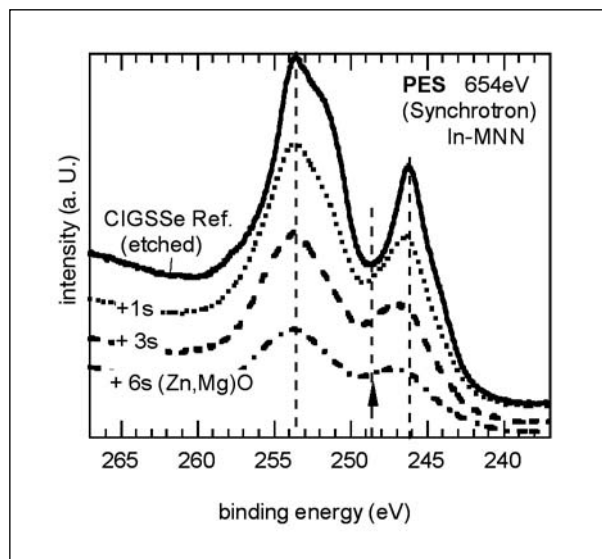


Fig. 2: Photoelectron spectra in the range of the In-MNN Auger electron. Compared to the spectrum of the clean chalcopyrite (CIGSSe), the local minimum shifts to higher energy and the shape of the main peak changes with deposition of (Zn,Mg)O, indicating oxidation of the Indium.

Novel approaches to the “lift-off” technology

S. Doka¹, D. Fuertes Marrón¹, K. Höhn¹, S. Lindner¹, A. Meeder¹, T. Münchenberg¹, M. Rusu¹, S. Wiesner¹, R. Würz¹, Th. Schedel-Niedrig¹, M. Ch. Lux-Steiner¹, K. Lips², W. Fritsch³, H. Bluhm⁴, M. Hävecker⁴, A. Knop-Gericke⁴, R. Schlögl⁴

■ 1 HMI, SE2 ■ 2 HMI, SE1 ■ 3 HMI, SF5 ■ 4 Fritz-Haber-Institut der MPG, Berlin

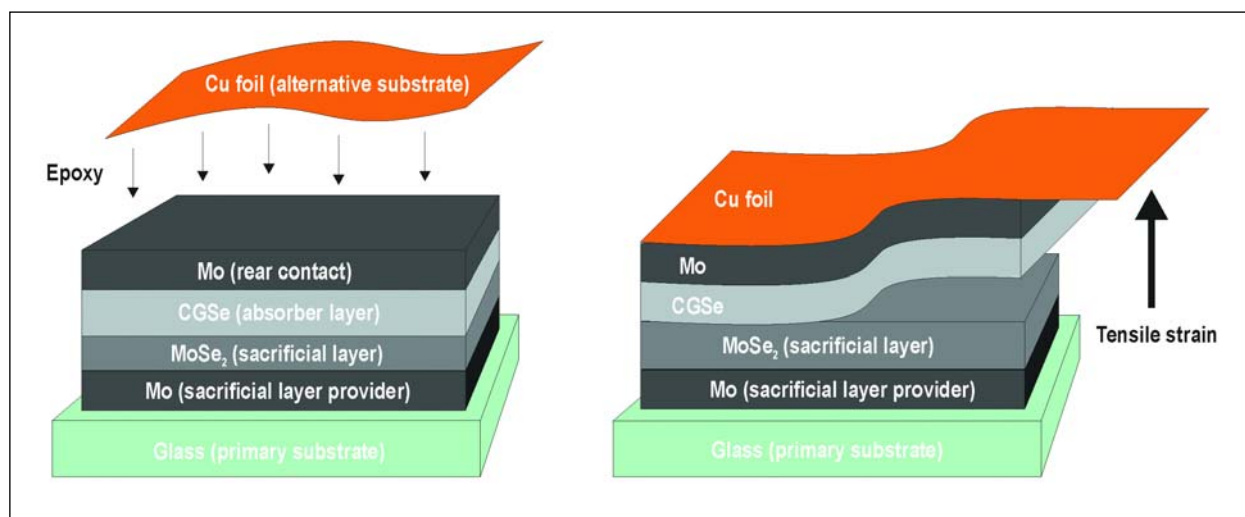


Fig. 1: Schematic view of the mechanical lift-off process proposed to transfer the thin-film CuGaSe_2 active layer to metallic foils.

The “lift-off” technique

The simultaneous formation of the layered chalcogenide MoSe_2 film between the Mo -rear contact and the absorber film during the CVD-growth of CuGaSe_2 thin films suggested a new approach to the lift-off process [1], which can be readily applied to these samples directly after the deposition process (Fig.1). Furthermore, no additional step is required in order to provide the sacrificial layer, as long as the MoSe_2 layer playing that role develops itself during the process. Indeed, the characteristic morphology, as revealed by TEM and XRD analysis [2], of the layers forming the MoSe_2 is nearly ideal for easily lifting the absorber layer off mechanically from its original Mo -coated glass substrate. The cleanliness (i.e. absence of substrate remnants on the absorber rear surface) was checked out by means of surface-sensitive techniques KPFM and XPS/UPS. First test devices on alternative substrates have been prepared (Fig. 2).

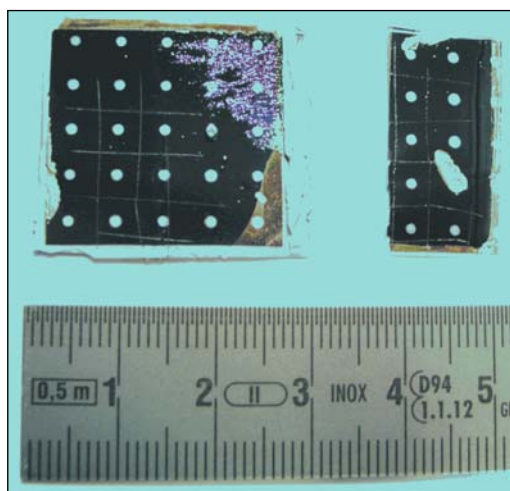


Fig. 2: CuGaSe_2 -based solar cells transferred onto flexible metal foils by means of a new lift-off process.

“Lifted-off” thin films for EPR-investigations:
An oxidation study of CuGaSe_2

The special bent structure of the interfacial MoSe_2 layer [3] permits a lifting-off of CuGaSe_2 thin films from the substrate simply by using adhesive tape (TESA®). X-ray fluorescence spectroscopy (XRF) doesn't reveal remnants of Mo on the backside of the lifted-off CuGaSe_2 film and also no traces of Ga or Cu on the substrate side are observed. Since the adhesive tape is Electron paramagnetic resonance (EPR) silent, EPR measurements on CuGaSe_2 thin films are therefore possible without any disturbing background signals from the substrate. The signal-to-noise ratio is enhanced by means of rolling up the film on the adhesive tape and placing it in quartz tube.

EPR measurements of CuGaSe_2 oxidized in air showed a broad Cu^{2+} signal (Fig. 3) [4]. It could be reduced to EPR silent Cu^+ by annealing in He atmosphere. Chemical etching with KCN removed this signal. In order to get insight into the chemical bonding state of the Cu^{2+} and the reaction pathway to non paramagnetic Cu^+ we performed core-level photoemission (XPS) on thin oxidized films. The formation of predominantly Ga_2O_3 and some amount of SeO_2 has been found at the surface-/near surface region after short term oxidation time for less than 4 month. Only after a long term oxidation process also $\text{Cu}^{2+}(\text{OH})_2$ was found (Fig. 4). This $\text{Cu}^{2+}(\text{OH})_2$ phase was reduced to Cu^+O^{2-} by vacuum annealing. Etching of the films in KCN removes the oxide phase. We therefore conclude that the EPR Cu^{2+} signal originates from a $\text{Cu}^{2+}(\text{OH})_2$ phase at the surface-/near surface region of the film.

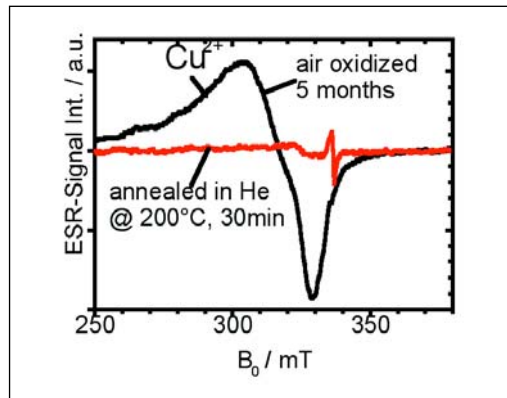


Fig. 3: EPR spectra of a CuGaSe_2 thin film

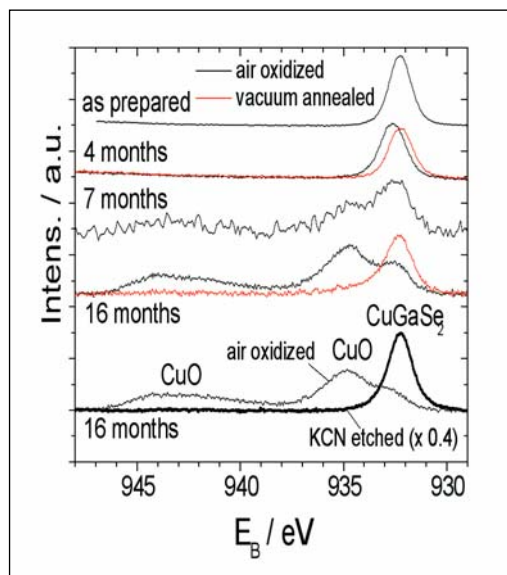


Fig. 4: $\text{Cu}2p$ -photoemission spectra of oxidized thin films

- [1] D. Fuertes Marrón, A. Meeder, Th. Schedel-Niedrig, R. Würz, M. Ch. Lux-Steiner, *Deutsches Patent für das Hahn-Meitner-Institut Berlin GmbH*, Deutsches Patent Nr. 102 47 735.B3, AT: 09.10.02, Patenterteilung: 15.04.04
- [2] D. Fuertes Marrón, A. Meeder, U. Bloeck, P. Schubert-Bischoff, N. Pfänder, R. Würz, S.M. Babu, Th. Schedel-Niedrig, M. Ch. Lux-Steiner *Thin Solid Films* **431–432**, 237–241 (2003).
- [3] R. Würz, D. Fuertes Marrón, A. Meeder, A. Rumberg, S.M. Babu, Th. Schedel-Niedrig, P. Schubert-Bischoff, U. Bloeck, M. Ch. Lux-Steiner *Thin Solid Films* **431–432**, 398–402 (2003).
- [4] R. Würz, K. Lips, et al., *Phys. Rev. B* (submitted)

Understanding of the ILGAR-WEL/CIGSSe interface

Ch.-H. Fischer¹, M. Bär¹, H.-J. Muffler¹, N. Allsop¹, C. Chapus¹, M.C. Lux-Steiner¹, S. Sadewasser¹, T. Glatzel¹, C. Kelch¹, M. Kirsch¹, L. Weinhardt², C. Heske², E. Umbach², F. Karg³, T. P. Niesen³

■ 1 HMI, SE2 ■ 2 Universität Würzburg, Experiment. Physik 2 ■ 3 Shell Solar GmbH, München

The main goal of the project is the further progress in chemical low-cost deposition methods for semiconductor thin layers, mainly the ILGAR process (Ion Layer Gas Reaction, patents by HMI). The Window Extension Layer Concept (WEL) allows the combination of buffer and intrinsic part of the window in one ILGAR-ZnO layer, i.e. one sputter step can be omitted.

Cells with ILGAR-ZnO WELs yield efficiencies (14.6 %) comparable to those with CBD-CdS (14.8 %) only on CIGSSe absorbers treated with Cd²⁺/NH₃. To improve the WEL cell performance and to make the device completely Cd-free, the interface modifications induced by the treatment have to be understood. Our earlier studies showing the purification effects of such a treatment, have been continued. In the X-ray emission spectrum of treated absorbers about a monolayer CdS could be identified by careful correction for the excess of CIGSSe (Fig. 1, spectra d and e). SEM plan views show no great difference between the bare and treated absorber surfaces (Fig. 2a, b). But on a bare surface the ILGAR-ZnO crystals are loosely arranged on the absorber facets, whereas the treated absorber surface acts as a seed layer and lets ZnO grow as a compact film consisting of very small crystallites and a few isolated larger particles (Fig. 2c, d). HRTEM images of cross-sections of both ZnO/CIGSSe samples confirm this difference in the nm-size regime (not shown here).

Kelvin probe force microscopy revealed a reduced local work function for the treated CIGSSe either due to a shift of the Fermi level towards the conduction band or due to a reduction in electron affinity. A distinction was possible by the combination of UV-photoelectron- (UPS) and inverse photoelectron spectroscopy (IPES) probing occupied and unoccupied states, respectively. The results for CIGSSe after various treatments led to the scheme of band positions in Fig. 3.

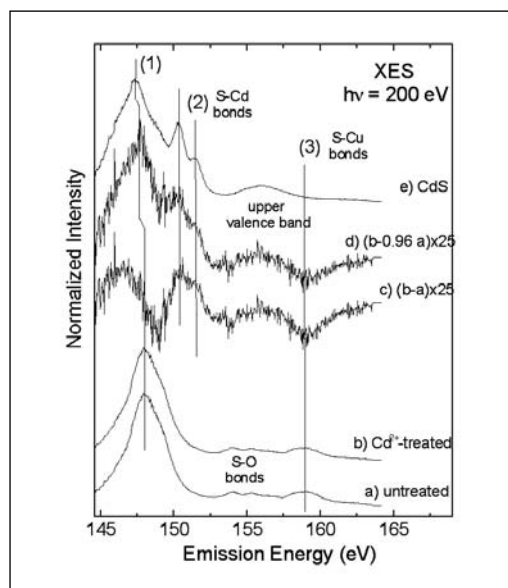


Fig. 1: S L_{2,3} XES spectra of untreated and Cd⁺ treated CIGSSe absorbers, difference spectra and CdS spectrum for comparison.

Only a few features can be stressed here:

- Fermi level shift towards conduction band by 0.4 eV after $\text{Cd}^{2+}/\text{NH}_3$ treatment.
- Band gap energy of untreated absorber 0.5 eV higher than for $\text{Cd}^{2+}/\text{NH}_3$ treated and sputtered one due to surface contaminations.
- Valence band maximum similar before and after $\text{Cd}^{2+}/\text{NH}_3$ treatment (1.00/1.10).
- Absorber surfaces are *n*-type (band bending! stronger for the $\text{Cd}^{2+}/\text{NH}_3$ than for the NH_3 treated one). Possible explanations: Cd^{2+} on Cu^+ vacancies or a CdS cover layer.
- Effect on band alignment of complete ILGAR-ZnO-WEL device: Change from spike to cliff at absorber/WEL interface due to $\text{Cd}^{2+}/\text{NH}_3$ treatment, therefore less recombination.

These effects on electronic properties, chemical composition, morphology and their influence on the growth of the ZnO-WEL explain the tremendous efficiency increase in the final solar cell by approx. one third when treated absorbers are used. Based on this knowledge a replacement of the Cd^{2+} in the treatment seems feasible.

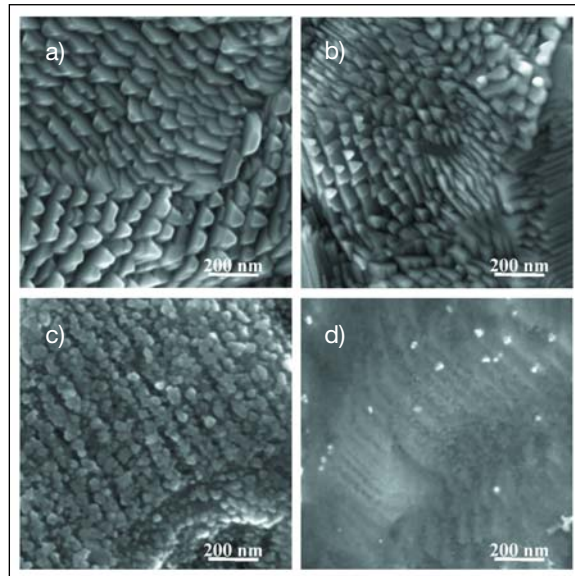


Fig. 2: SEM plan view of bare a) and $\text{Cd}^{2+}/\text{NH}_3$ treated b) absorber as well as of ILGAR-ZnO on top of untreated c) and $\text{Cd}^{2+}/\text{NH}_3$ treated d) CIGSSe.

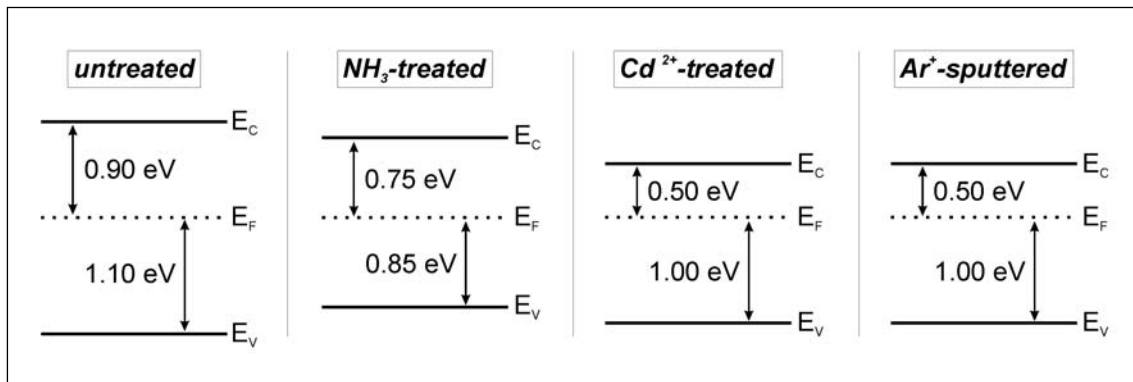


Fig. 3: Schematic band edge positions of an untreated, NH_3 and $\text{Cd}^{2+}/\text{NH}_3$ treated as well as sputtered CIGSSe surface (from left to right).

Over 11 % efficient $ZnS/CIGSSe$ thin film solar cells without undoped ZnO

A. Ennaoui, S. Sartale, B. Sankapal, T. Kropp, M. Lux Steiner

■ HMI, SE2

Goal: The objective of this research is to identify, explore, evaluate, and develop a non-vacuum process capable of making a breakthrough in the production of low cost thin-film chalcopyrite solar cells. This includes robust processing compatible with Cd-free $Cu(In,Ga)SSe_2$ (CIGSSe) thin film solar cells. To date chalcopyrite thin film emerging technology is based on CdS as a buffer layer. Elimination of CdS layer has the potential benefits of improved carrier collection in the shorter wavelength portion of the spectrum as well as reduced manufacturing waste. The present focus is on a new chemical method, of producing thick films consisting of ZnS-clusters. We adopted a coordination chemistry method to grow ZnS from colloids. The process labelled ZnS-Colloid Based Materials (ZnS-CBMs) is more efficient and cost-effective. Furthermore in contrast to standard chemical bath deposited ZnS (CBD-ZnS) presented in our previous reports [1]; there is no need to complex the Zn-cation with N_2H_2 , which is highly toxic. The structure of ZnS layers is found to be of spherulite (tetrahedrally coordinated cubic ZnS) along (111) directions.

Device performance: A series of CIGSSe devices was fabricated where the CdS layer was replaced by the new chemically deposited ZnS-CBMs. Solar cells in this study were fabricated with production scale absorbers made at Shell Solar Munich. Highly doped sputtered Ga:ZnO was directly sputtered onto CIGSSe/ZnS surface without need of undoped ZnO. Fig. 1 shows SEM (cross section) of the ZnO/ZnS/CIGSSe device structure. The conformal coverage of the absorber is obvious and the thickness of ZnS-CBMs was estimated to be around 30 nm. Fig. 2 shows the output characteristic of the solar cell. The best solar cell with ZnS-CBMs is compared in efficiency to the CdS reference device (table 1). The outcome of main interest in this work is that there is no need to have undoped ZnO and devices show low performance and greater crossover between light and dark JV curves in their as-deposited state than for devices after heating and soaking. The highest performance is obtained after annealing in Argon atmosphere at 200°C and light soaking at 25°C for 40 min.

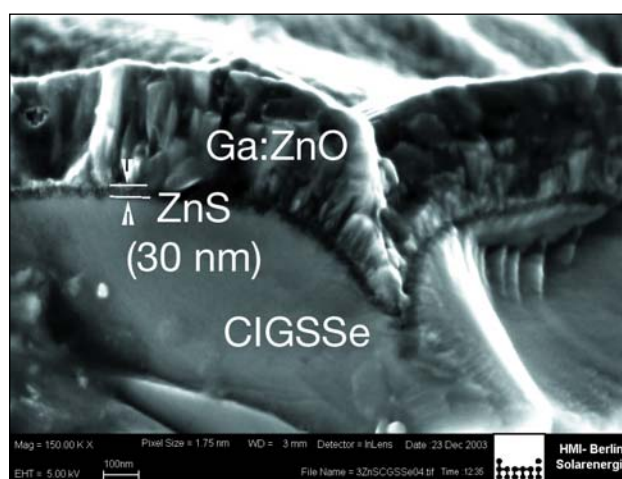


Fig. 1: Scanning Electron Micrographs (Cross section) of the Ga:ZnO/ZnS/CIGSSe structure

With the new ZnS-CBMs the light soaking effect is rather strong. The reason for this strong effect after annealing and light soaking requires further investigation. Ongoing work will investigate this issue.

Conclusion: A new strategy has been used to develop a robust process for Cd-free CIGSSe solar cells. We adopted a coordination chemistry method to grow ZnS colloids instead of using a standard CBD with highly toxic complexing agents. Obviously ZnS-CBMs process has competitive performance compared to cells made with a CdS layer and the undoped ZnO layers in CIGSSe devices is not essential. Device efficiency over 11 % was found by eliminating CdS and undoped ZnO.

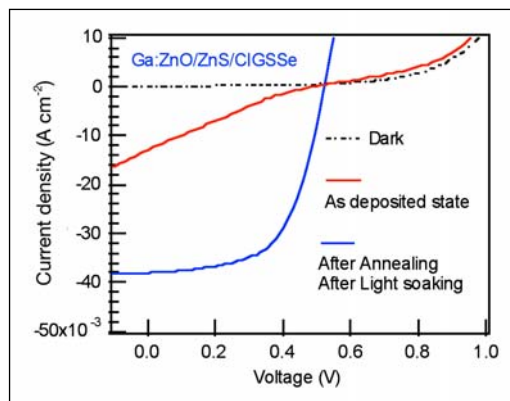


Fig. 2: J-V characteristics of the ZnS/CIGSSe thin film-based solar cell without the undoped ZnO.

- [1] Ennaoui, A.; Eisele, W.; Lux-Steiner, M.; Niesen, T.P.; Karg, F., *Highly efficient Cu(Ga,In)(S,Se)₂ thin film solar cells with Zinc-compound buffer layers*, Thin Solid Films **431–432**, 335–339 (2003).

Barrier	V _{oc} [mV]	J _{sc} [mA/cm ²]	FF	η [%]
Cds ref.	530	33.1	62.7	11.0
ZnS no-ALS	490	12.9	22	1.41
ZnS ALS	522.45	38	58.7	11.69

Table 1: PV parameters of CIGSSe solar cells. With CdS (ref.), before annealing and light soaking (no-ALS), after annealing and light soaking (ALS)

Coherent manipulation of well-defined electron spins in solid state

C. Meyer¹, W. Harneit¹, B. Naydenov¹, K. Lips², A. Weidinger¹

■ 1 HMI, SE2 ■ 2 HMI, SE1

The size of electronic devices decreases steadily. Current research aims at devices built upon small structures or even single molecules making use of quantum mechanical properties, e.g. spins. In our group we want to make use of the spin dynamics of the endohedral fullerenes $N@C_{60}$ and $P@C_{60}$ in molecular spin electronic devices such as a quantum computer. Because the C_{60} fullerene shields the endohedral nitrogen or phosphorus atom from the environment, these molecules have exceptional spin properties, e.g. long electron spin relaxation times [1].

The cross-section of a fullerene with a group V endohedral atom is shown schematically in Fig. 1. The atom resides at the centre without any bonding to the fullerene molecule. The valence electrons of the half-filled p-shell couple to a spin $S = 3/2$. Using a solid-state ensemble of these molecules, the net-magnetisation can be measured and manipulated with pulsed electron spin resonance (ESR).

In a transient nutation experiment, the spins are rotated by a well defined angle depending on the pulse length t_p of the first pulse shown in Fig. 2. The detection is done in the x,y -plane, thus, a second pulse is needed for the read-out. If the spin states “up” and “down” are taken as logic “true” and “false” (or 1 and 0), a 180° pulse changes the information from 1 to 0 and vice versa, thus performing a NOT operation.

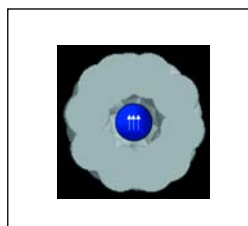


Fig. 1: Schematic cross-section of a fullerene. The Van der Waals radii are shown for the carbon atoms. The three valence electrons of the encapsulated nitrogen or phosphorous couple to a total spin $S = 3/2$.

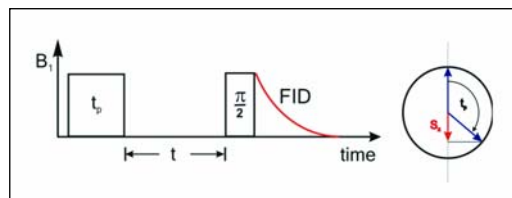


Fig. 2: ESR pulse sequence of a transient nutation experiment. The microwave field B_1 is applied perpendicular to the external field B_0 . The spins are rotated by a certain angle depending on the pulse length t_p of the nutation pulse. The S_z component of the spins is rotated into the measurement plane by a $\pi/2$ -pulse.

For strong fields B_1 , the spins of the endohedral fullerenes behave like an $S = 1/2$ system. In Fig. 3 we show the transient nutation signal for $P@C_{60}$ (a) and $N@C_{60}$ (b) powder samples. For better illustration the data have been multiplied with an exponential function so that decay due to spin-spin relaxation is not visible. The experiment has been carried out at room temperature and is a good illustration for the exceptionally long spin lifetimes. Up to 50 (30) coherent oscillations can be measured for $N@C_{60}$ ($P@C_{60}$).

For $P@C_{60}$ it is possible to excite the $(1/2, -1/2)$ transition and the $(\pm 3/2, \pm 1/2)$ transitions separately at low temperatures. If the B_1 field is sufficiently small (much smaller than the zero-field-splitting $D \sim 6$ G), the transitions will rotate with different frequencies, due to the different transition elements in the S_+ operator for a $3/2$ -spin.

As can be seen from equation (1) the expected

$$S_+ = \begin{pmatrix} 0 & \sqrt{3} & 0 & 0 \\ 0 & 0 & 2 & 0 \\ 0 & 0 & 0 & \sqrt{3} \\ 0 & 0 & 0 & 0 \end{pmatrix}$$

ratio of the nutation frequency of the $(1/2, -1/2)$ transition and the $(\pm 3/2, \pm 1/2)$ transitions is $2/\sqrt{3}$.

The nutation experiment at $T = 10$ K shown in fig. 4 clearly reveals this ratio. We thus could demonstrate that we have full control over the $S = 3/2$ spin system.

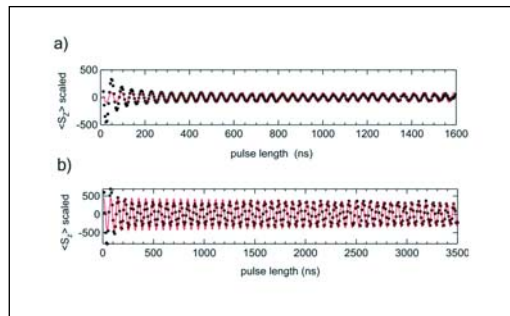


Fig. 3: Data (black) and fit (red) of the transient nutation experiment with a) $P@C_{60}$ and b) $N@C_{60}$.

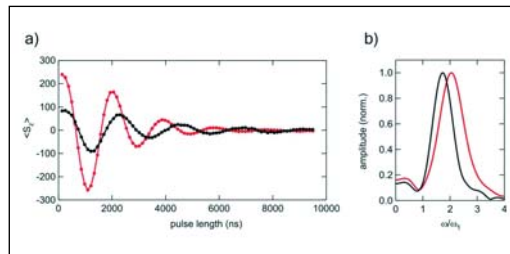


Fig. 4: a) Transient nutation of a $P@C_{60}$ powder sample at $T = 10$ K. The read line shows the $(1/2, -1/2)$ transition while the black line shows the $(3/2, 1/2)$ transition. b) The Fourier transform of the transient nutation signal clearly reveals the different frequencies.

[1] T. Almeida Murphy, T. Pawlik, A. Weidinger, M. Höhne, R. Alcalá, J.-M. Spaeth, Phys. Rev. Lett. **77**, 1075 (1996).

CuAlO₂ prepared from LiAlO₂ by ion exchange reaction

L. Dloczik¹, Th. Dittrich¹, T. Guminskaya¹, N. Grigorieva¹, M. Ch. Lux-Steiner¹, Y. Tomm² in cooperation with I. Urban³
 ■ 1 HMI, SE2 ■ 2 HMI, SE5 ■ 3 BAM

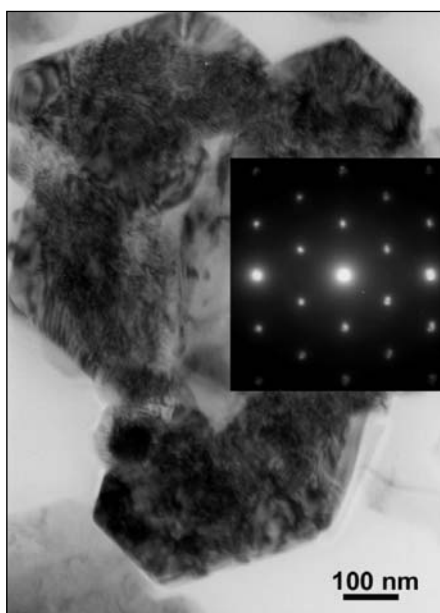


Fig. 1: Micrograph crystallites and electron diffraction pattern of CuAlO₂ obtained from LiAlO₂.

The delafossite phase of CuAlO₂ is a promising inorganic transparent hole conductor with a band gap of about 3.5 eV. However, there are only few and high temperature technologies available to prepare CuAlO₂. We showed that LiAlO₂ can be used as a precursor to produce CuAlO₂ by an ion exchange reaction at moderate temperatures [1].

The mobile Li-ions in the α -LiAlO₂ phase are exchanged by copper ions. This is possible because both phases have the same rhombohedral lattice structure (R3m)

of layered M-O-Al-O (M corresponds to Li or Cu) and because Al-O bonds are very stable.

For the preparation, a powder of α -LiAlO₂ and the double molar amount of CuCl was placed into a glassy carbon boat and heated for several hours in a sealed quartz tube under high vacuum at temperatures around 400 – 500°C. The by-product LiCl and remaining CuCl were washed out and the reaction product was analyzed by electron microscopy, x-ray diffraction, reflectance spectroscopy and photovoltage spectroscopy.

Figure 1 shows small crystallites of CuAlO₂ which are formed after ion exchange at 475°C. A photovoltage spectrum of a layer consisting of small CuAlO₂ crystallites is presented in Figure 2. The photovoltage response was characteristic for *p*-type semiconductors. The band gap is 3.54 eV and the energy of the exponential states is 50 meV at room temperature. This and the absence of deep states in the

forbidden gap demonstrate the high quality of the prepared CuAlO₂.

The obtained CuAlO₂ crystallites are very stable in air and vacuum. They have been covered by different absorber layers. It has been shown that hole injection takes place from dye molecules into CuAlO₂ under illumination. An important challenge is now to find methods for further technological processing of the CuAlO₂ crystallites for various applications.

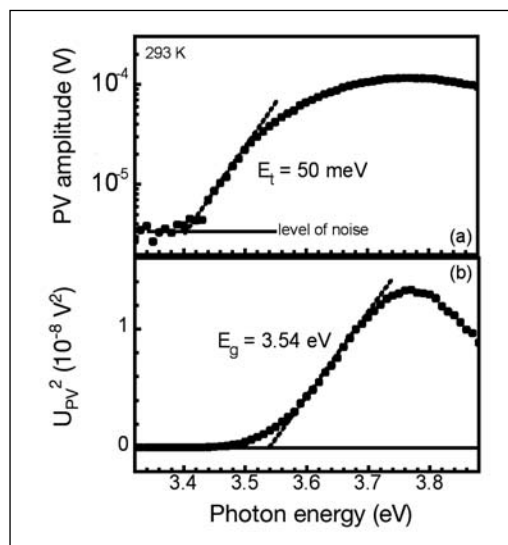


Fig. 2: Photovoltage spectra of a layer of small CuAlO₂ crystallites.

- [1] L. Dloczik, Y. Tomm, Th. Dittrich, M. Ch. Lux-Steiner, *Verfahren zur Herstellung von CuAlO₂ unterhalb von 500°C durch Kristallstrukturkonforme Austauschreaktion*, Patent, pending

Vertical nanowire field effect transistor in flexible template

J. Chen¹, R. Könenkamp¹, S. Klaumünzer²
 ■ 1 HMI, SE2 ■ 2 HMI, SF4

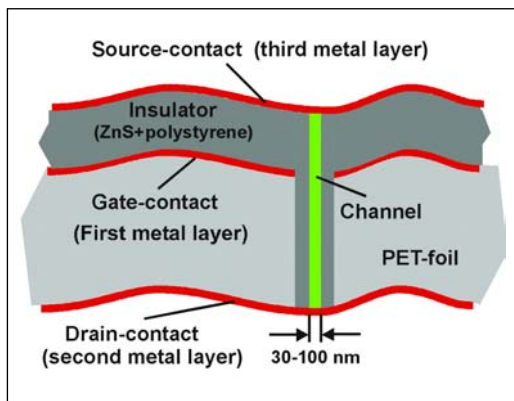


Fig. 1: Structure of a vertical nano-wire transistor

The fabrication of nanowire transistors has spurred considerable activity in material science, nanotechnology and in logic architectures. One approach to attain these goals is based on the use of hybrid structures combining the flexibility of organic materials as substrates with the device functions of inorganic semiconductors. To take full advantage of the small dimensions of nanowire devices, a vertical orientation is, however, more desirable, since in the vertical geometry packing densities up to 10^{10} cm^{-2} appear feasible. A stacking of vertical transistor layer may even lead to higher densities. Eventually reconfigurable architectures will allow a large degree of randomness in densely packed structures, thereby opening the possibility that these device structures may also be used in logic applications.

A vertical device structure with a packing density of $\sim 10^7 \text{ cm}^{-2}$ recently has been realized by us [1], but the fabrication scheme and the observed large gate leakage current, limited the usefulness of this first experimental approach. However we have succeeded in fabrication of improved version of vertical nanowire transistors in flexible template. The device structure is illustrated in Fig. 1. The new device is also more robust and exhibits a strongly reduced gate leakage current. Similar to our earlier design the fabrication involves a sequential

deposition of metal, insulator and semiconductor layers on a nano-structured polymeric template, consisting of a flexible self-supporting PET foil. The channels were produced by etching tracks of swift heavy ions from ISL. The first metal layer works as the gate contact. When the channel-diameter is small enough, the potential induced by the gate contact reaches radially through the whole channel and a large conductance variation between source and drain contacts can be achieved (cf. Fig. 2). Switching and amplification become possible.

The transistors are operated in the hole depletion mode with a reduced transconductance at negative gate voltages. At present the conductance variation is $\sim 50\%$ for gate voltages between $\pm 2 \text{ V}$. The leakage current density is typically less than 1% of the source-drain current. Applications of this type of transistor in flexible optical displays appear feasible. Replacement of the source, drain and gate contacts by horizontal nanowires may eventually open the way to the addressing of single transistors in a three terminal mode. As the fabrication process allows a stacking of the foil arrays at high packing density is achievable. With these prospects we understand our results as a proof-of-concept that will initiate further research on materials, techniques and device structures for this type of hybrid device.

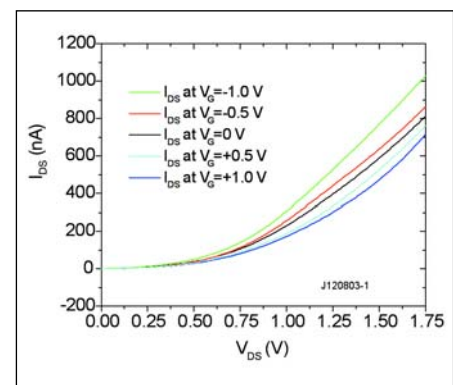


Fig. 2: Source-drain current vs. source-drain voltage of an array of about 1500 vertical field-effect-transistors. Parameter is the gate voltage V_G .

[1] J. Chen, R. Könenkamp, *Applied Physics Letters*, **82**, 4782 (2003).

* J. Chen, R. Könenkamp, *Vertical nano-wire field effect transistor in polymer foils*, European patent Nr.: 10142913, US: 5981970, JP: 11-329334, JP: 61-4017

Synchrotron-based characterization of industrially relevant chalcopyrite solar device structures

Ch.-H. Fischer¹, M. Bär¹, A. Grimm¹, H. Jungblut¹, I. Kötschau¹, I. Lauermann¹, H.-J. Lewerenz¹, K. Rahne¹, J. Reichardt¹, K. Skorupska¹, S. Sokoll¹, M.C. Lux-Steiner¹, L. Weinhardt², O. Fuchs², C. Heske², C. Jung³, W. Gudat³, T. P. Niesen⁴, S. Visbeck⁴, F. Karg⁴

■ 1 HMI, SE2 ■ 2 Exp. Physik II, Universität Würzburg ■ 3 BESSY GmbH, Berlin ■ 4 Shell Solar GmbH, München

The aim of the CISSY project is the investigation of buried interfaces and surfaces in chalcopyrite thin film solar devices by means of synchrotron-based spectroscopy. In the following example the use of x-ray emission spectroscopy (XES) for the identification of secondary phases on a CuInS_2 -absorber is shown.

In the HMI baseline process for the preparation of CuInS_2 -absorbers an excess of copper precursor compared to the stoichiometric composition is necessary to obtain the required crystal quality and electronic properties. However, this results in the formation of a secondary, electrically conducting Cu_xS (mainly CuS) surface phase which has to be removed in order to produce efficient solar cells. This removal is usually achieved by selective etching in a KCN solution. As the use of KCN is undesirable in an industrial process, alternative ways of removing Cu_xS are sought. One method, developed by Lewerenz et al. [1], is an electrochemical (EC) etch, which removes most of the Cu_xS . However, solar cells built with the initially developed method had efficiencies below 3%. Since, in photoelectron spectroscopy, chemical shifts of the copper peaks between CuInS_2 and Cu_xS are small, it was at first unclear, whether any residual Cu_xS (possibly Cu_2S), remained on the surface. EC etching of CuS is known to initially form Cu_2S [1]. The surface sensitivity of x-ray diffraction in this case is too low to resolve the matter.

Therefore, XES was utilised to examine the CuInS_2 -absorber surfaces after different EC etches. XES is based on the excitation of core level electrons with soft X-ray radiation and subsequent fluorescence caused by the relaxation of valence electrons into the core holes. The chemical environment of the emitting atoms is thus reflected in specific spectral features due to the varying contributions of neighbouring atoms to hybridized valence states. Thus, different compounds containing the same element will have specific XES spectra.

Spectra were recorded in the CISSY end station with the XES-300 X-ray spectrometer (Scienta Gammadata) at the U41-PGM beam line at the BESSY synchrotron. $\text{S-L}_{2,3}$ spectra from EC etched samples are shown in Fig. 1, together with spectra from the as-grown sample, a KCN-etched absorber, and a Cu_2S reference. Comparison of spectrum (D) of an EC etched surface to that of the KCN-etched reference (C) reveals small differences in the upper valence band area above 153 eV. Analysis suggests that Cu_2S (shown in (E)) is present on the surface. Based on these results, the etching procedure was modified, leading to a surface that gives rise to spectrum (B), which is almost identical with the reference spectrum (A). This is verified by computing the difference spectrum (G). Furthermore, solar cells fabricated with the new procedure reach an efficiency of 8%. This example shows the value of XES to give chemical information which is complementary to results from other spectroscopic techniques and to assist in the development of state-of-the-art thin film solar cells.

[1] M. Aggour, U. Störkel, C. Murrell, S.A. Campbell, H. Jungblut, P. Hoffmann, R. Mikalo, D. Schmeisser, H.J. Lewerenz, *Thin Solid Films* **403–404**, 57 (2002).

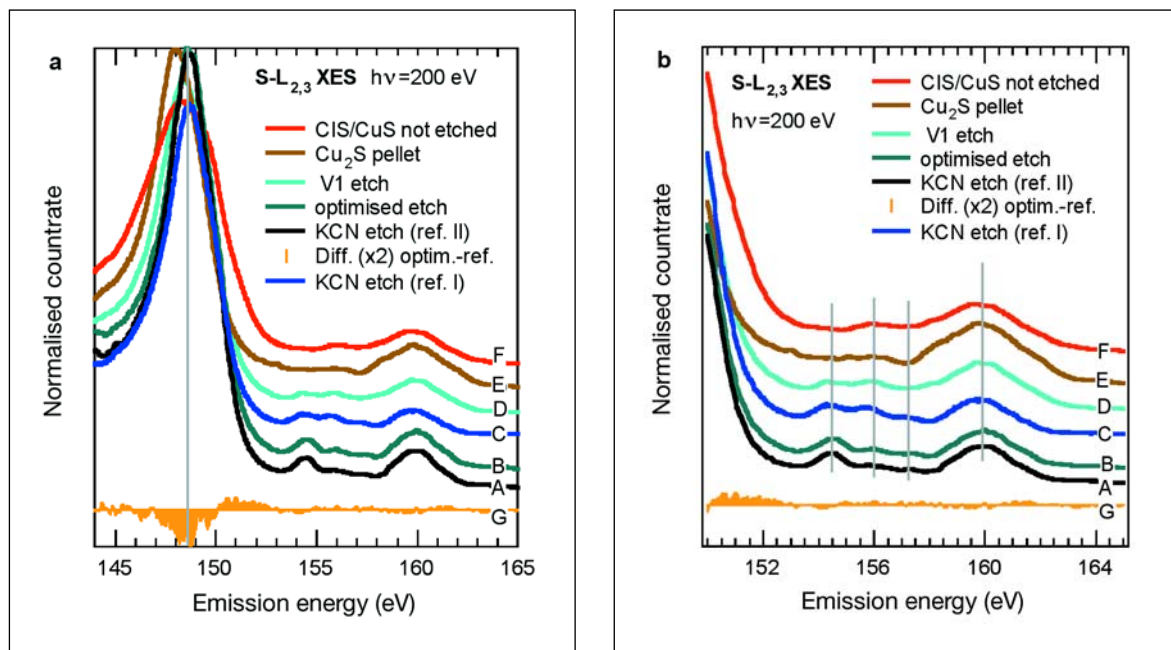


Fig. 1: a) S- $L_{2,3}$ X-ray emission spectra of a CuInS_2 (CIS) sample etched with KCN (A, C), an as-deposited CIS sample (F), a Cu_2S reference (E), an electrochemically etched CIS sample (old procedure, (D)), and a sample etched according to a new procedure (B). G is the difference between spectrum B (optimised procedure) and spectrum A (reference KCN-etched sample). Spectra (B) and (A) were recorded with a different detector than (C) to (F).

b) Enlarged detail of spectra showing the transitions from the upper valence band into S 2p holes. Vertical lines designate spectral features related to S-In bonds (154-158 eV) and S-Cu bonds (160 eV).

Solar cell cross section studied by Kelvin Probe Force Microscopy in ultrahigh vacuum

Th. Glatzel, H. Steigert, N. Barreau, P. Carl, S. Sadewasser, M.Ch. Lux-Steiner, D. Fuertes-Marrón,

Th. Schedel-Niedrig

■ HMI, SE2

Kelvin probe force microscopy (KPFM) in ultrahigh vacuum allows to simultaneously obtain structural as well as electronic information (work function Φ) of a sample's surface with an extremely high lateral (~ 20 nm) and energy resolution (~ 5 meV).

An important issue for improving the performance of solar cells is an appropriate electronic band alignment at the various interfaces of the different layers that compose a CuGaSe_2 heterostructure. Typical chalcopyrite thin film solar cells consist of a Mo back contact on soda lime glass, the p -type absorber layer, a thin buffer layer and a n -type window layer. We present UHV-KPFM measurements on a cross section through a complete solar cell structure [1]. With this method we recorded absolute work function values of the different material surfaces forming the device. Detailed information was obtained especially on the interfaces after the optimization of the sample cleaning process in UHV. The cross section of the chalcopyrite solar cell was prepared by gluing two devices face-to-face and polishing with aluminum paste (grain size ~ 20 nm).

Due to polishing and cleaning in air, we expect the surface to be covered with adsorbates, inducing surface defects. This results in a reduced contrast in contrast potential (CP) of only 100 meV between the different layers. Therefore, the sample was subsequently cleaned by several soft sputtering processes using Ar-ions (500 eV) under 45° incident angle in UHV.

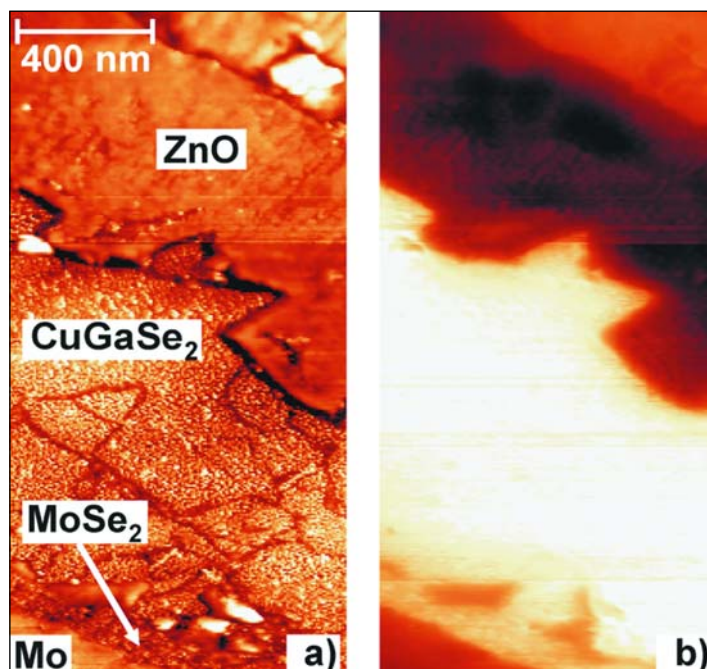


Fig. 1: Image of a CuGaSe_2 solar cell cross section (1000×2000 nm²) after 60 min Ar-ion sputtering (500 eV): a) topography (color scale = 65 nm) and b) work function ($\Phi = 3.92 - 4.86$ eV).

The topography (a) and the work function (b) of the sample after 60 min sputtering are shown in Figure 1. Due to the different sputtering rates of the materials a topographical contrast between the layers is observed. From the bottom of the images the Mo back contact, the chalcopyrite absorber (CuGaSe_2), and the ZnO window layer on the top can be seen. The work function image shows a clearer contrast of up to 570 meV between the different layers under dark conditions, and up to 700 meV under illumination. Between the absorber and the Mo back contact an additional layer of about 100 nm thickness with a distinct work function is observed. We attribute the additional contrast between Mo and absorber layer to an MoSe_2 intermediate layer. This is in agreement with recent high resolution transmission electron microscopy and scanning energy dispersive X-ray detection measurements which show the formation of an interfacial MoSe_2 layer with a thickness of 150 nm. The Mo/ MoSe_2 interface is an intimate contact formed during the deposition process. For the MoSe_2 /absorber interface we observe some voids in the interface, related to a non-homogeneous nucleation process of the crystallite seeds during the absorber deposition.

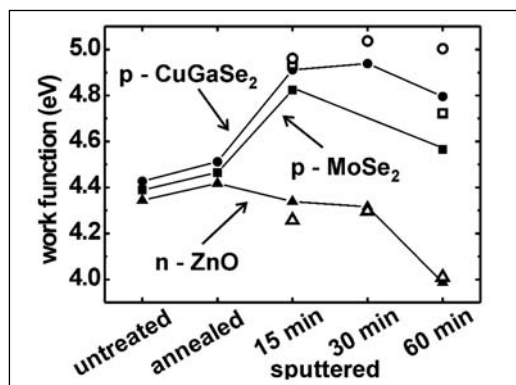


Fig. 2: Work function of the different materials in a CGSe solar cell after different surface treatments. The open symbols represent the values under super band gap illumination ($\sim 60 \text{ mW}$, $\lambda = 442 \text{ nm}$).

An overview of the work function values of the different materials in dependence on the cleaning step is presented in Figure 2. The open symbols function of the absorber and the MoSe_2 layer changes under illumination to higher values; the illumination reduces the band bending at the p -type semiconductor surface. Upon further increase of the illumination intensity we observed no significant change in the work function, we assume that we achieved nearly flat band conditions at the surfaces. Under these conditions and after 15 min Ar-sputtering, the work function of CuGaSe_2 is 4.96 eV. For the highly n -doped ZnO we determine a work function of 4.26 eV. In Figure 2 it can also be seen, that up to a sputtering time of 30 min only the p -type semiconductors change the work function significantly. Due to the high carrier concentration of ZnO ($n \approx 10^{21} \text{ cm}^{-3}$) the effect of adsorbates on the position of the Fermi energy at the surface should be minimal. For longer sputtering times a significant reduction of the work function of all layers was measured. We attribute this to a change in the surface stoichiometry, caused by preferential sputtering of some elements. In Figure 1 the formation of clusters on the absorber surface can be seen. We relate these to metallic Ga which reduces the work function of the CuGaSe_2 surface. Despite this, the absorber layer reaches a nearly constant value under illumination for sputtering times up to 60 min.

- [1] Th. Glatzel, D. Fuertes-Marrón, Th. Schedel-Niedrig, S. Sadewasser, M. Ch. Lux-Steiner, Appl. Phys. Lett. **81**, 2017–2019 (2002).

Chalcopyrite solar cells on flexible substrates

A. Neisser, Ch. Kaufmann, R. Klenk, R. Scheer

■ HMI, SE3

It is one of the inherent advantages of a thin film technology, that – in principle – it can be deposited on any kind of foreign substrate. So far, however, thin film solar cells are usually deposited on glass substrates. In a joint project of SE3 and SE2 the glass substrate is to be replaced by a 25 μm thick titanium foil. The resulting solar cells will then be light weight, flexible and almost unbreakable! Furthermore, with >1000 Watts/kilogram, the high specific power of such solar cells opens up completely new areas of applications for thin film photovoltaic devices, for example in solar arrays for satellites in space or airborne vehicles. An additional advantage of chalcopyrite solar cells with respect to space applications is their excellent hardness to a radiative environment (protons and electrons). A prerequisite for these applications is a high solar-to-electric conversion efficiency of >15 % at AM1.0.

The layer structure of a $\text{Cu}(\text{In,Ga})\text{Se}_2$ solar cell on titanium foil is shown in Figure 1. The crucial $\text{Cu}(\text{In,Ga})\text{Se}_2$ layer is prepared by physical vapor deposition using a sequential, three-stage co-evaporation process. On a laboratory scale (device area = 0.5 cm^2) the project team has reached an efficiency of 16.7 % on glass substrates. For this process, an *in situ* process control (using laser light scattering) has been developed and patented. This laser system has demonstrated high potential.

In a next step the preparation process had to be transferred from a glass substrate to a thin film metallic foil suitable for space applications. Special attention had to be paid to the increased surface roughness of a metallic foil compared to a glass substrate. It was found that substrate irregularities introduced local defects in the device structure, which primarily limited the performance of the final device. By introducing an additional substrate conditioning step this limitation, however, could be overcome (see Figure 2).

To date conversion efficiencies of reference cells on titanium are comparable to efficiencies on glass (see Table 1). The targeted efficiency of 15 % for a space dedicated device has already been realized on a small area of 0.5 cm^2 . Efficiencies of more than 12 % have been reached on larger areas of up to 16 cm^2 (Table 1), which represents a world record efficiency for a flexible thin film solar cell with an area larger than 1 cm^2 .

Cells have also been tested under reverse voltage bias. Such stress tests are essential with respect to module integration where partial shading of individual cells can impose high current loads on these cells. Samples have been tested under reverse bias of up to -3.0 V for 30 min. The maximum current had been limited to -1.0 A , which corresponds to more than twice the short circuit current of these cells. It could be found that all samples show a reverse breakthrough which is fully reversible. Right after the reverse bias test the open circuit voltage is lower by only about 40 mV. The cell fully recovers under illumination at open circuit conditions. The initial efficiency is reached again after around 1 hour. That means that flexible CIGSe cells can be integrated in a solar cell module without any need for additional bypass diodes commonly used in existing technologies.

Current activities focus on 1) investigating the feasibility of the unique process control for in-line deposition processes, 2) identifying physical and technological reasons for the gap in device performance between small area and large area single cells and 3) increasing the area of the single cell device from 16 cm^2 to 32 cm^2 . Furthermore, the group will be involved in a test program (in cooperation with Dutch-Space and ESA) dedicated to investigate the potential of its thin film solar cells for future space application.

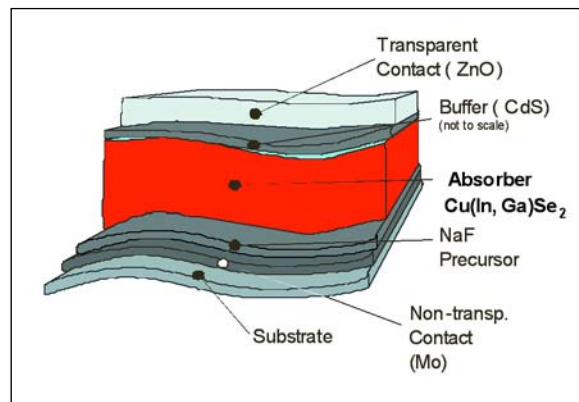


Fig. 1: Layer sequence of flexible solar cell.

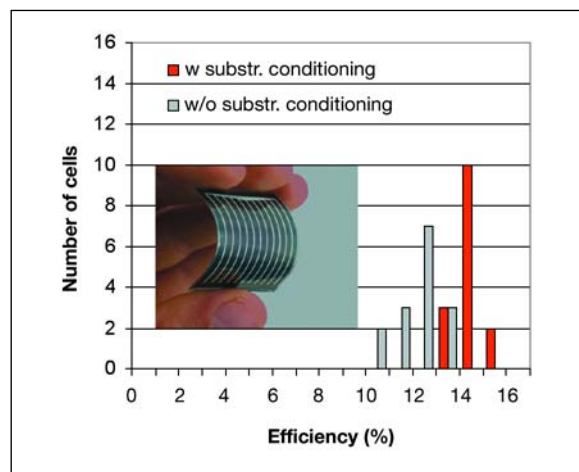


Fig. 2: Distribution of efficiencies of small area devices on a $40 \times 40 \text{ mm}^2$ substrate. Inset: Flexible solar cell based on Cu(In,Ga)Se_2 (area 16 cm^2).

	area (cm^2)	V_{oc} (mV)	ff (%)	j_{sc} (mA/cm^2)	η (%)
glass	0.5	661	75	33.8	16.7
Ti	0.5	636	76	33.6	16.2
Ti	16	624	71	27.5	12.2

Table 1: Record efficiency of flexible solar cells on Ti-foil (reference on glass included for comparison).

About the mechanism of CuInS_2 film formation

Ch. Pietzker, R. Scheer

■ HMI, SE3

The formation of CuInS_2 absorber layers for solar cells by use of a sequential process is within the centre of research of the technology department. The growth initiates from metallic Cu, In layers and intermetallic compounds such as CuIn_2 , $\text{Cu}_{11}\text{In}_9$, and $\text{Cu}_{16}\text{In}_9$. Addition of sulphur and heating of the substrate leads to the transformation into the chalcopyrite structure. In the case of CuInS_2 absorber layers, Cu-rich precursor layers are used resulting in a Cu-S phase as a byproduct.

The temperature profile for the sulphurisation normally includes a ramp-up phase, a holding phase, and a cool-down phase. Typical substrate temperatures in the holding phase are 500°C . The question of the investigation in the following presented is: What is the dominant kinetic limitation for the sulphurisation process? In order to answer this question, *in situ* XRD experiments during the sulphurisation have been performed. The precursor layers have been pre-annealed and transformed into the intermetallic phase $\text{Cu}_{16}\text{In}_9$. Therefore, for the present experiments the sulphurisation starts from the phase $\text{Cu}_{16}\text{In}_9$. No further intermetallic phase transformations occur during the temperature cycle. The inset in Fig. 1 shows a sketch of the layer structure at an intermediate state. Part of the $\text{Cu}_{16}\text{In}_9$ layer has been consumed and has been converted into CuInS_2 . It is known that the growth front of CuInS_2 is at the front surface of the CuInS_2 layer. This implies that Cu and In atoms have to pass the preliminary CuInS_2 layer by diffusion. At the surface they react with sulphur.

A standard method for the investigation of diffusion processes is isothermal annealing and quantification of educts and products. Fig. 1 (top) shows a temperature profile for an annealing experiment at 375°C . Initially, the substrate temperature is fastly ramped to the annealing temperature. At this temperature, the annealing phase is followed. After the end of the annealing phase, the substrate temperature is ramped to the top value (600°C). Fig. 1 (bottom) shows the $\text{Cu}_{16}\text{In}_9$ XRD peak intensity as a function of time for different annealing experiments. $\text{Cu}_{16}\text{In}_9$ is the educt of the reaction. It should be emphasised that this intensity is complementary to intensity of the product

CuInS_2 . We see in the figure that $\text{Cu}_{16}\text{In}_9$ is consumed in the ramp period of the experiment at 375°C but not in the isothermal holding period. The same is valid for the XRD intensities of isothermal experiments at other temperatures. There, the isothermal period lengths have been altered. Obviously, the consumption of $\text{Cu}_{16}\text{In}_9$ and the growth of CuInS_2 mostly takes place in the ramp-up periods and only to a minor extend in the holding period. In other words, growth of CuInS_2 mainly follows a temperature law and not a time law.

In a different experiment series, this result has been confirmed: Using an identical top temperature, different ramp rates have been applied and the consumption of $\text{Cu}_{16}\text{In}_9$ as well as the formation of CuInS_2 have been investigated. It was found that growth of CuInS_2 is always finished at the end of the ramp-up period. We interpret this effect as a stress-induced growth mechanism: Due to the difference in the expansion coefficients of $\text{Cu}_{16}\text{In}_9$ ($\alpha = 3.3 \times 10^{-5} \text{ K}^{-1}$) and CuInS_2 ($\alpha = 0.9 \times 10^{-5} \text{ K}^{-1}$), a tensile stress is induced within the CuInS_2 layer. This stress may be released by the formation of microcracks or grain boundaries. It is assumed that the diffusion of Cu and In atoms takes place along the cracks or is promoted by stress within the CuInS_2 top layer. Similar growth mechanisms had been reported for the oxidation of metal layers [1].

We compared the growth of Cu-rich CuInS_2 layers with Cu-poor layers of CuInS_2 as well as with CuInSe_2 layers. In neither of the latter cases a similar growth mechanism has been found. The result of this study is particularly important for the CuInS_2 solar cell process. It allowed to omit the holding period in a sulphurisation experiment. Thereby, the process time can be reduced in favour of a higher throughput in production.

[1] H.E. Evans, Int. Mat. Rev. **40** (1), 1-40 (1995).

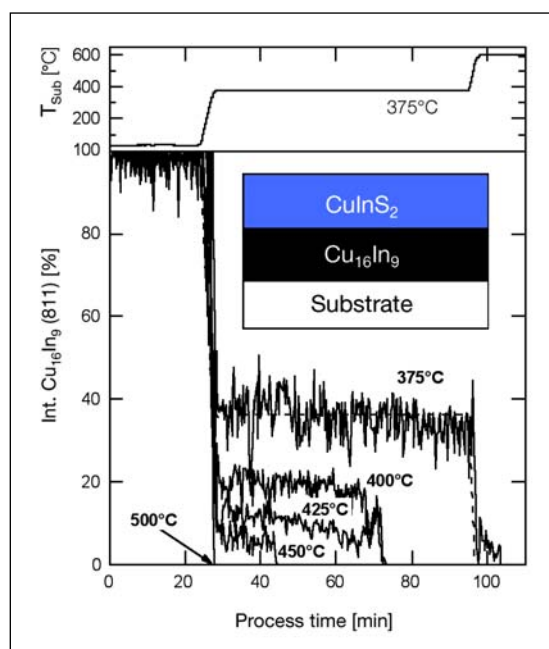


Fig. 1: (bottom) XRD intensities of the phase $\text{Cu}_{16}\text{In}_9$ as a function of process time for different temperature profiles for sulphurisation. (top) Exemplarily, the temperature profile for an experiment at 375°C is given. It includes fast ramp periods at 25 min and 95 min process time and a holding period of 60 min at 375°C . Similar are the experiments at 400°C , 425°C , 450°C , and 500°C , however, with shorter holding periods. The inset shows the layer sequence of an intermediate stage of the sulphurisation.

Local diode parameters determined by infrared thermography

I. Gavilanes-Pérez, R. Scheer

■ HMI, SE3

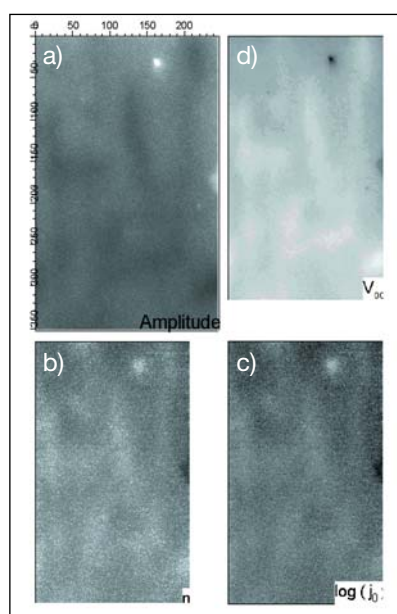


Fig. 1: a) Image of the IR amplitude at 0.74 V forward bias. Brightness proportional to current density. b) Calculated images of the spatial diode quality factor n , c) saturation current density $\log(j_0)$, and d) open circuit voltage V_{oc} of a standard Mo/CuInS₂/CdS/ZnO solar cell. The sampled area is $2.5 \times 4 \text{ mm}^2$. The scale gives the pixel number.

Solar cells and modules are large area devices for which the coherent action of every cell segment is of paramount importance. A defected module area of micrometer size can deteriorate the performance of up to 100 cm^2 cell area. Defects can be a result of inhomogeneous cell processing or of inherent variations of the diode parameters. Up to now, little is known about the spatial homogeneity of chalcopyrite thin film solar devices. A quantity of particular relevance is the open circuit voltage V_{oc} and its lateral homogeneity. Recent PL mappings of device-grade Cu(In,Ga)Se₂ devices revealed a variation of the quasi-Fermi level splitting of 10 meV measured at 70 K [1]. It is clear that this quantity can be translated into a variation of the open circuit voltage ΔV_{oc} . Furthermore, this variation should be larger at room temperature.

By use of lock-in thermography we calculated ΔV_{oc} for the first time from the spatial dark current density of chalcopyrite cells. Solar cells of the area 0.5 cm^2 were set in front of a IR camera. This camera allows to sample the emitted heat of the cell with $10 \times 10 \text{ }\mu\text{m}^2$ spatial resolution. A forward bias voltage was applied to the cell. Due to the high conductivity of the front and back contact, it can be assumed that the voltage is homogeneously imposed on all cell areas. According to the local current-voltage characteristic of each cell element, the current density at each element may vary. An element with a shunt or a weak diode, for instance, will carry a higher current density. Thus it will dissipate more energy which is detected

by the IR camera. Fig. 1 gives an example of an amplitude image recorded at a bias of 0.74 V. The x and y axes denote the pixel numbers. At the pixel number (165,30) a shunt is revealed by higher brightness of the image.

Images of the emitted heat are recorded for different voltages. They form a matrix of values for the dissipated power as a function of voltage for each cell element. From this a matrix of current density as a function of the voltage can be calculated. As a result, the diode characteristic for each cell element is achieved. This diode characteristic can be evaluated in terms of the diode quality factor, n , and the saturation current density, $\log(j_0)$. Finally, n and j_0 can be plotted as a gray scale image.

Fig. 1 exemplarily shows maps of n and j_0 for a CuInS₂ solar cell. Higher values of n and j_0 are represented by increased brightness. A cloudy variation of both parameters can be discerned. As is theoretically expected, areas of higher n values correspond to areas of higher $\log(j_0)$ values. If the n factor values from the thermography experiment are mathematically averaged over the sampled area, a value of $n = 1.6$ with a FWHM of 0.4 is achieved. The peak value is identical to the n -factor resulting from the electrical jV measurement.

The diode quality factor and the saturation current density are two quantities which determine the open circuit voltage of a device. Assuming homogenous light current generation, the V_{oc} can be easily calculated and plotted as an image. This is done in Fig. 1. A cloudy structure complementary to the amplitude image but congruent to the $\log(j_0)$ image is obtained. Only the shunt at (165,30) has a contrast differing from the $\log(j_0)$. The variation of the open circuit voltage ΔV_{oc} over the cell area is about 50 mV. A similar ΔV_{oc} value we found for a Cu(In,Ga)Se₂ device. Thus the thermography data are in agreement with PL measurement.

[1] K. Bothe, G. H. Bauer, and T. Unold, Thin Solid Films **403–404**, 453–456 (2002).

Experimental proof for MOCVD-specific surface reconstruction of InP(100)

T. Letzig, H.-J. Schimper, T. Hannappel, F. Willig
 ■ HMI, SE4

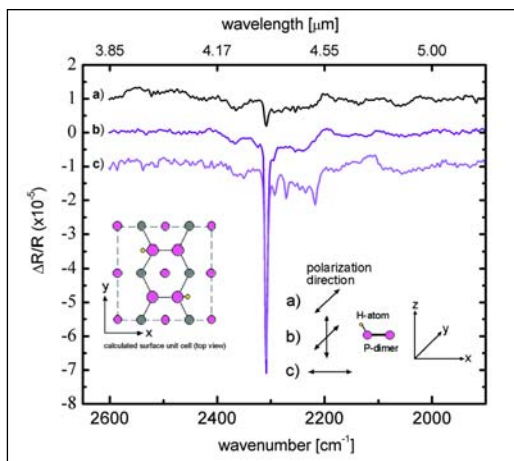


Fig. 1: Three IR difference spectra of P-H stretching vibrations at different polarizations of the incident light. For clarity, there is an arbitrary shift in vertical direction.

Metalorganic vapor deposition (MOCVD) is the method of choice for industrial growth of III-V semiconductor layers, i.e. for binary materials like GaAs and InP, and also for ternary and quaternary variants. The MOCVD growth technique is based on thermal decomposition of metalorganic precursor molecules such that a highly pure and ordered phase of the III-V solid is left behind on a suitable substrate. The method requires a proper preparation procedure and must be carried out in a suitable MOCVD reactor. For specific industrial purposes and in particular for basic science the growth of such materials is carried out without precursor molecules, just making use of the III-V chemical elements (MBE). A recent theoretical hypothesis has postulated that hydrogen will be incorporated into a specific P-rich ordered surface reconstruction of InP(100) if the material is grown via MOCVD [1]. A completely different ordered surface should be formed as the P-rich reconstruction when the material is grown via MBE. The theoretically postulated surface unit cell of the P-rich reconstruction prepared via MOCVD is characterized by a phosphorous dimer whose dangling bonds are stabilized via formation of one P-H bond (compare inset on the left hand side of Fig. 1).

We found direct experimental proof for the postulated surface reconstruction in the form of INFRARED spectra measured in ultra-high-vacuum at the MOCVD grown surface (Fig. 1). The specific IR peak showed the polarization dependence expected to arise for the theoretically proposed surface unit cell with the P-H bond. The result was achieved making use of a unique sample transfer system mounted at the exit of our MOCVD reactor. The latter provides sample transfer into UHV without suffering any surface contamination or further reconstruction. Each spectrum shown in Fig. 1 represents a difference spectrum based on a measurement carried out prior to and another after removal of all the P-H bonds from the as-grown surface. The latter state was achieved via a sufficiently thorough exposure to deuterium gas. Correspondingly, the P-H vibrations at the as-grown surface appeared in the difference spectrum as a strong negative peak in Fig. 1 with wavenumber at 2308 cm^{-1} ($= 4.33\text{ }\mu\text{m}$). Polarization of the impinging light beam in y-direction did not excite this particular vibration (spectrum a). This was expected from the theoretical model (inset at the left) since the dipole moment of the P-H vibration should not show a component in this direction (compare also the inset at the lower right hand side of Fig. 1). In contrast, there was a strong peak (spectrum b) and c) when the impinging light was polarized parallel to the x-z plane where the dipole moment of the P-H vibration has been predicted in the theoretical model. Our complete FTIR data give the first direct experimental proof for the MOCVD-specific P-rich surface reconstruction of InP(100) [2]. The latter is strikingly different from the surface reconstruction of the P-rich surface prepared via MBE. Making use of our patented MOCVD-UHV sample transfer the MOCVD prepared surface was investigated in the absence of any post-transfer preparation step.

- [1] P.H. Hahn, W.G. Schmidt, *Surf. Rev. Lett.*, **10**, 163 (2003)
 [2] T. Letzig, H.-J. Schimper, T. Hannappel, F. Willig, submitted to *Phys. Rev. B*

Energy distribution of hot electrons in a semiconductor exposed to sunlight

M. Neges, K. Schwarzburg, F. Willig

■ HMI, SE4

Theoretical scenarios for various types of solar cells with potential solar conversion efficiencies higher than can be reached with a conventional one-band gap solar cell (so-called 3rd generation photovoltaic devices) go back more than 20 years. A specific postulate has addressed the collection of hot charge carriers at a suitable electrical contact material [1]. The corresponding theoretical postulated scenario involved a thermal distribution of hot charge carriers prepared via absorption of sunlight by the semiconductor. The distribution was characterized by a temperature parameter of several thousand degrees. The above postulate has remained a topic in the photovoltaic literature until today [2]. Surprisingly, the postulate has never been checked experimentally or via a realistic model calculation. Recently, we have addressed this question both experimentally and by a model calculation.

Experimental fingerprints of the hot electron dynamics were measured at He temperatures in InP as characteristic dips in the excitation spectrum of the photocurrent collected at a transparent hetero-contact (InP/SnO₂) (Fig. 1). Such dips are known to arise from the enhanced recombination probability when hot electrons reach exactly the bottom of the conduction band via a series of emission processes for LO-phonons (cascade). Electrons with negligible kinetic energy show the highest probability for capture by recombination centers.

The corresponding dips in the photocurrent excitation spectrum were reproduced in a Monte Carlo simulation of hot electron dynamics that incorporated all the relevant scattering processes for hot electrons and their respective temperature dependence (Inset Fig. 1). The Boltzmann transport equation (BTE) was solved by means of Monte Carlo techniques for electrons that were optically generated in the conduction band. The energy range of < 0.4 eV above the lower conduction band edge was addressed in the simulations allowing for a parabolic approximation of the conduction band dispersion. Scattering with LO-phonons, acoustic phonons, impurities, and holes was considered. Conduction band to acceptor recombination was used as the dominant recombination path. The charge separating hetero-interface was mimicked as an infinite sink. The simulation was based on the above experimental data and extrapolated to room temperature.

The energy distribution of hot electrons impinging on the contact is shown in Fig. 2 for *p*-doped InP for both medium and small dopant concentrations. Clearly, the spikes in the calculated distributions for the energy of the hot electrons that reach the contact are highly non-thermal (thermal distributions are indicated for comparison). This is in stark contrast to the assumptions in the earlier theoretical scenario of Ross and Nozik. Implications of these results for solar cells based on the collection of hot carriers at the contact will be investigated further based on the above realistic hot electron dynamics.

-
- [1] R. T. Ross and A. J. Nozik, *J. Appl. Phys.* **53**, 3813 (1982).
[2] P. Würfel and T. Trupke, *Physik Journal* **2**, (12), 45 (2003).

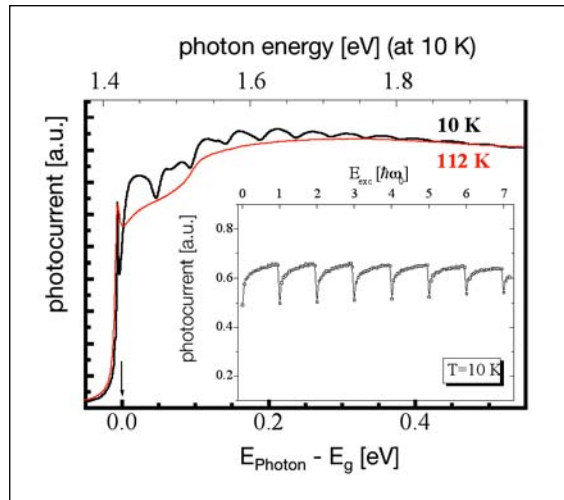


Fig. 1: Photocurrent excitation spectra at 10 K and 112 K. Hot electrons provide the excess photocurrent at low temperatures. Inset: Monte-Carlo-simulation of the photocurrent.

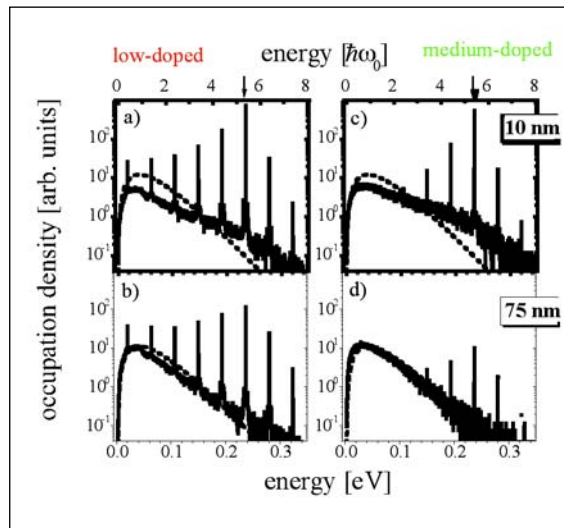


Fig. 2: Energy distribution for hot electrons that reached the contact from a starting distance of 10 and 75 nm, respectively. Note the logarithmic scale of the ordinate. The electrons were generated at room temperature with 234 meV kinetic energy above E_{CB} .

Solar cells with small band gaps built from III-V materials

H.-J. Schimper, U. Seidel, T. Hannappel, K. Schwarzburg, F. Willig
 ■ HMI, SE4

Hitherto the highest solar conversion efficiencies have been achieved with multi-junction cells of III-V materials, where the smallest band gap, however, is realized with a different type of material. The record example of a triple-junction cell with 36.9 percent conversion efficiency is the combination InGaP/GaAs/Ge [1]. Band gaps greater than 1.35 eV can be realized with III-V materials whose lattice constants are close to that of GaAs. Smaller band gaps, however, require III-V materials with lattice constants similar to that of InP. In principle a small band gap cell, e.g. 1 eV, can be realized also with the lattice constant of GaAs, requiring the quaternary material GaInAsN. Unfortunately, corresponding efforts have not yet resulted in an N-containing III-V material that would show a satisfactory minority carrier diffusion length.

In contrast, the present project aims at preparing a triple-junction solar cell where also the small band gaps are realized with III-V materials based on the lattice constant of InP and do not require Nitrogen to be incorporated. With the band gap combination of 0.75 eV (InGaAs), 1.15 eV (InGaAsP) and 1.7 eV (InAlAsSb) the optimum efficiency for a triple-cell can be realized.

The triple-junction cell is prepared in consecutive steps, first suitable mono-junction cells are being grown, next a double-junction cell is developed, etc. The mono-junction cell InGaAs with band gap 0.74 eV was prepared and showed a solar conversion efficiency of 8.5 percent. The mono-junction cell InGaAsP with band gap 1.2 eV showed an efficiency of

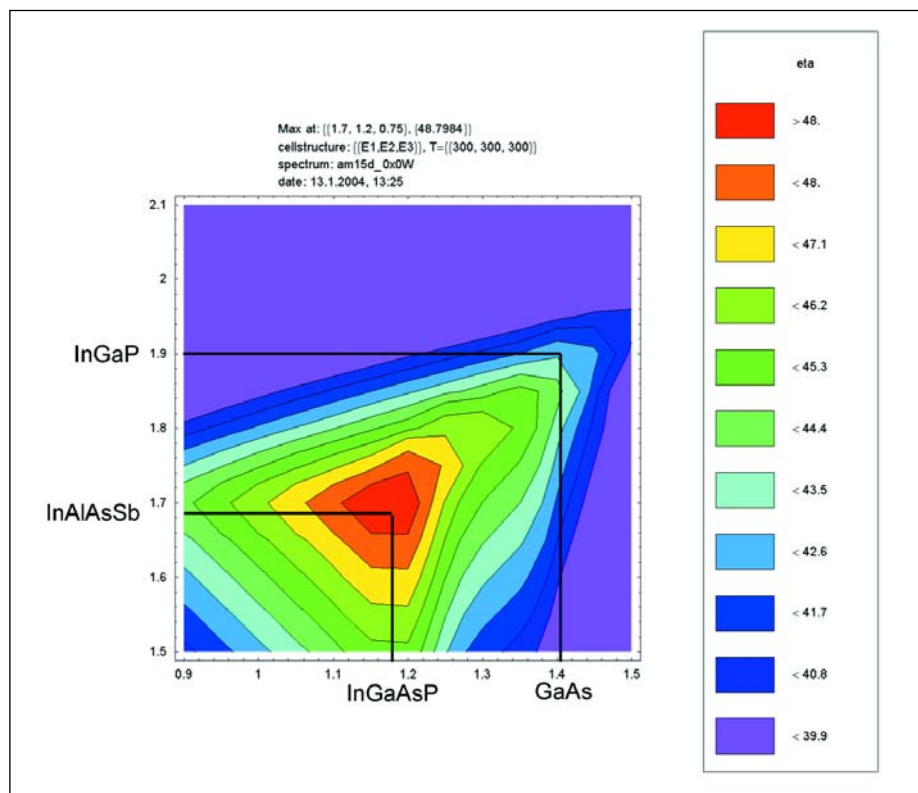


Fig. 1: Efficiencies for Triple-junction-cells with two variable bandgaps for the top cells. The band gap for the bottom-cell is fixed at 0.75 eV (InGaAs or Ge)

11.3 percent. Both the cells were measured without anti-reflective (AR) coating. GaAsSb was grown with band gap 0.72 eV as alternative to InGaAs. For improving the conversion efficiency several specific preparation steps have to be implemented, one of them is photolithography. The latter facilitates mesa-etching and a lift-off technique for the preparation of the electrical contacts. This technique yields a well-defined active cell area and a well-characterized area for the electrical contacts. The former is better defined compared to contact formation via evaporation of the metal through a shadow-mask. The grid of the electrical contact can be prepared with a smaller distance between neighboring metallic strips resulting in a reduced series resistance. Compared to the same InGaAs mono-junction cell where the electrical contacts were formed via shadow-mask metal-evaporation photolithography has increased the conversion efficiency from 6.5 to 8.6 percent.

A single-layer anti-reflection coating (AR) has improved the external quantum efficiency of an InGaAs solar cell from 65 percent to 85 percent, with a corresponding increase in the conversion efficiency from 6.5 percent to 8.5 percent. The AR coating was not yet effective over the whole active spectral range and thus has to be improved further. Photolithographic preparation of the electrical contacts (compare above) is expected to raise the conversion efficiency of this cell further.

[1] King RR et. al. *Lattice-matched and metamorphic GaInP/GaInAs/Ge concentrator solar cells*. Proceedings of the World Conference on Photovoltaic Energy Conversion (WCPEC-3), Osaka, May 2003

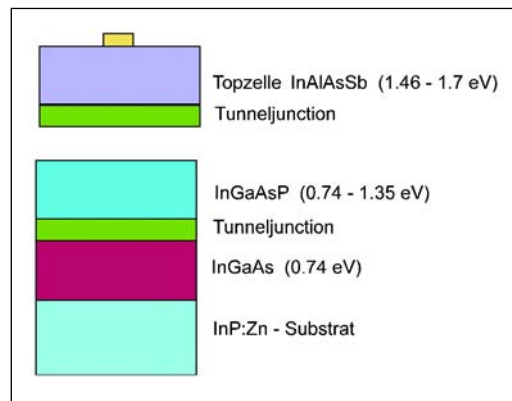


Fig. 2: Triple-junction cell on an InP substrate

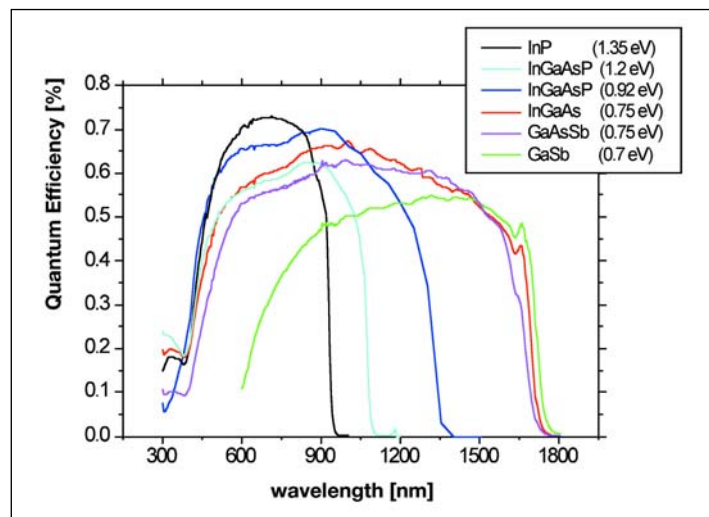


Fig. 3: External Quantum Efficiencies of single-junction-cells on InP

Chemical Surface Modification of Molybdenum-, Tungsten-Dichalcogenides for Optimal Photoeffects

A. Barkschat, H. Tributsch

■ HMI, SE5

Well-grown molybdenum- and tungsten-dichalcogenide crystals (MoX_2 with $X = \text{S}, \text{Se}, \text{Te}$) in contact with aqueous electrolytes (wet solar cells) have yielded solar energy conversion efficiencies exceeding 15 %. Efforts, however, to produce solar cells in the form of thin layers or sintered powders failed because the photoeffects deteriorated due to the participation of unfavorable crystal surfaces perpendicular to the Van der Waals interface of the two-dimensional materials (for a review see [1]). These surfaces exhibit reactive chemical bonds, which serve as recombination centers and orbitals for undesired interfacial chemistry. In order to take advantage of the abundant and environmentally friendly compounds MoS_2 and WS_2 for thin layer and composite solar cells, research towards neutralization of these recombination centers became necessary.

A useful tool for this study of photo-induced interfacial processes became imaging techniques for photocurrents (Fig. 1) [2].

They clearly show that even crystals grown of these compounds exhibit a variety of surface sites with different energy conversion properties. This is shown in Fig. 1 by applying different potentials to the photo-absorber in contact with a liquid iodide-triiodide electrolyte. While at short circuit conditions (Fig. 1, left) high photocurrents flow, they systematically decrease towards the open circuit potential (Fig. 1, right). It is recognized that different areas of the crystal behave differently and thus show different power output characteristics and different fill factors.

Studies were initiated to identify compounds which selectively interact with dangling transition metal bonds perpendicular to the layer structure. One of the best compounds investigated up to now, which positively influences such an interface is the detergent TWEEN 80. After the surface is treated with a 4 % aqueous solution of this compound for three hours, the photocurrent output is clearly improved. This is seen in Fig. 1b, which shows that this most significant effect is an improvement of the power output characteristic for different areas. This can be seen in the increased photocurrent density near the open circuit voltage (Fig. 1a and 1b, right sides).

One complication in the interpretation derives from the observation that the effects are very anisotropic. This indicates that there is a large variety of different surface conditions for which the effect of the detergent may have somewhat different results. Photoelectrochemical and also microwave-photoelectrochemical measurements are on the way to get more detailed information. It is expected that systematic research on the interaction of selected chemicals with layered-type semiconductor particles will lead to the development of nano- and polycrystalline solar cells made of these materials.

[1] A. Aruchamy (Ed.), *Photoelectrochemistry and Photovoltaics of Layered Semiconductors*, Kluwer Academic Publishers, Dordrecht (1992).

[2] A. Barkschat, PhD-Thesis, Freie Universität Berlin (2003).

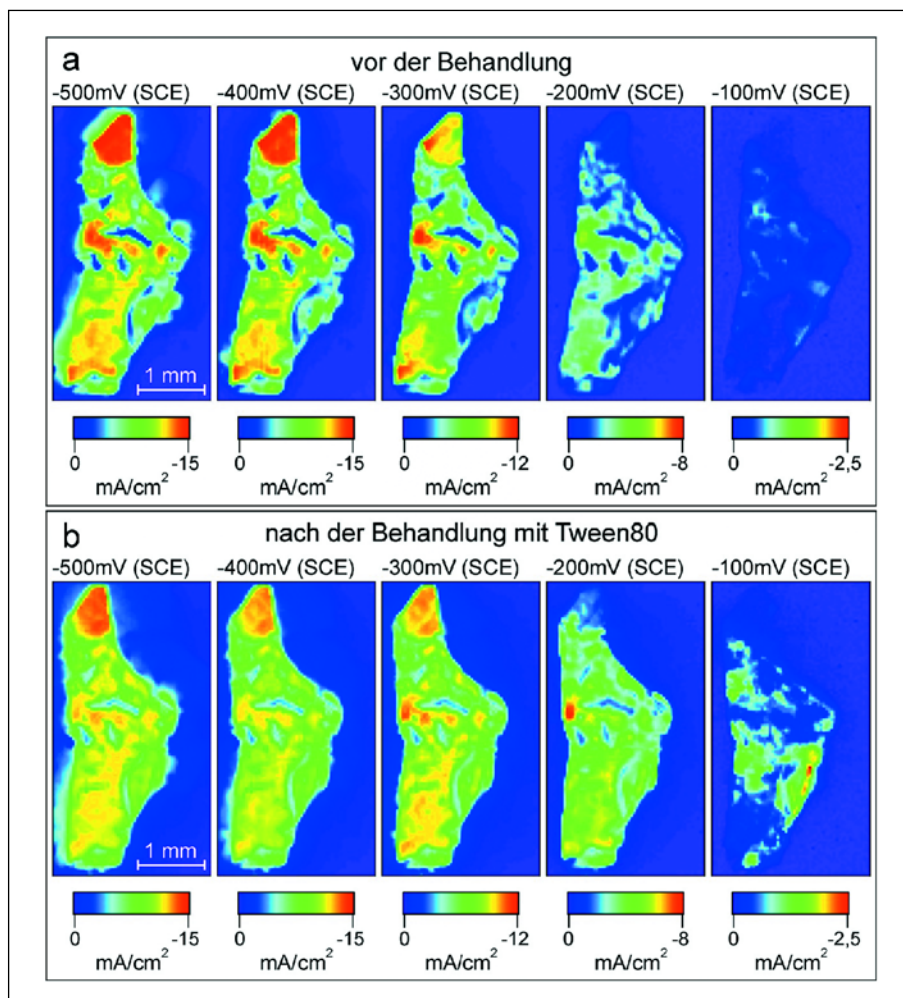


Fig. 1: shows photocurrent images of a p-WSe₂ crystal, in contact with a redox electrolyte measured at different electrode potentials, from short circuit (left) towards open circuit conditions (right). The original light to photocurrent conversion conditions (a) are clearly improved upon surface treatment with Tween 80 (b), especially towards open circuit conditions (right). [2]

Noble metal free catalysts for the electro-reduction of oxygen

S. Fiechter, P. Bogdanoff, G. Schmithals, I. Herrmann, I. Dorbandt, H. Tributsch

■ HMI, SE5

Introduction.

In processes converting chemical into electrical energy under clean environmental conditions, the development of the polymer electrolyte membrane fuel cell (PEM-FC) system plays a central role. However, to introduce PEM-FCs as a mass product, the nowadays used platinum-based catalysts have to be replaced by abundant transition metals.

Preparation and characterisation of catalysts.

Recently, it has been demonstrated that iron-cobalt catalysts, prepared by pyrolysis using a mixture of metal porphyrins (e.g. CoTMPP) and oxalates (e.g. FeC_2O_4) or employing carbon particles (BP) impregnated with porphyrins in an inert gas, led to electrocatalysts reducing oxygen with an efficiency comparable to platinum [1–3]. In some cases, catalytic activity is further enhanced by the addition of sulphur to the precursor. The novel catalyst exhibits a highly porous carbon structure [1–2]. Although neutron activation analysis showed Fe- and Co-concentration of less than 2wt %, no metal particles of nanometer size could be detected neither by scanning nor by transmission electron microscopy nor by x-ray diffractometry. Therefore, it was assumed that the catalytic centres must consist of metal clusters or atoms integrated into the surfaces of the in-situ formed carbon support by pyridinic-type nitrogen [4].

EXAFS measurements. Extended X-ray Absorption Fine Structure (EXAFS), measured at the k-edges of cobalt and iron in carbon-supported catalysts of $\leq 2\text{wt} \%$ metal content revealed that two metal centres are present consisting of single iron or cobalt atoms, integrated in a carbon matrix via nitrogen bridges. Since the metal-nitrogen distance is identical with that found in crystalline porphyrins it is supposed that also the symmetry of the nitrogen coordinated metal atom remains unchanged.

Figure 1 shows the magnitude of Fourier-transformed EXAFS functions for the following samples: metallic cobalt (red curve), cobalt tetramethoxyphenyl-porphyrin CoTMPP (blue), heat treated CoTMPP without acid treatment (light green) and two catalysts (CoTMPP/ iron oxalate) with (orange) and without sulphur after acid treatment (dark green). The peak at 2.43 Å corresponds to the Co-Co distance of metallic cobalt (red). Pure CoTMPP exhibits a peak at 1.7 Å (blue). This value is corroborated with the Co-N distance in the chelate structure. Since the curves are not phase corrected the atomic distances found are smaller than those known from x-ray single crystal structure analysis. The curve of the heat treated CoTMPP (light green) exhibits dominant Co-Co distances while the Co-N peak is significantly reduced. It can be concluded that most of the chelate-cores are destroyed during pyrolysis and that elementary cobalt is formed. To efficiently remove the catalytic noneffective metallic particles from the heat treated samples it has been demonstrated that the addition of iron oxalate and sulphur leads to a foamed catalyst structure [2–3] where the metallic components easily could be removed by acid treatment. The sulphur-free curve (orange) closely resembles the pure porphyrine curve at the Co-N peak position but does not exhibit the typical features of the next ligands: porphyrine decomposes but a fraction of the Co-N_4 cores remains unchanged embedded in the carbon matrix. The course of the EXAFS curves originating from samples prepared by adding sulphur and those measured at the iron edge show similar features (dark green).

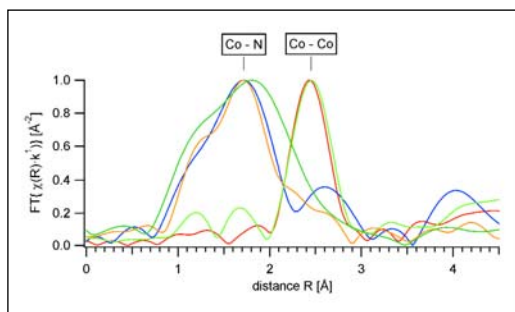


Fig. 1: Magnitude of the Fourier-transformed EXAFS functions (normalized without phase correction).

Electrochemical and surface characterisation.

Electrochemical activity of the catalysts were determined in a 0.5 M H_2SO_4 electrolyte using rotating ring disc electrodes under oxygen purging [2]. These electrochemical experiments were carried out in a three-electrode-system employing a saturated mercury sulfate electrode. Figure 2 shows kinetic currents of differently prepared catalysts related to the electrode surface versus voltage, calculated from Koutecky-Levich equation (Tafel-plots). Best results were obtained using a $\text{CoTMPP}/\text{FeC}_2\text{O}_4/\text{S}$ precursor. However, the high current densities of carbon-supported Pt catalyst (20wt % Pt on carbon) used as reference has not yet been achieved. It was found that high catalytic activity of the new catalysts is correlated with the surface area, determined by sorption measurements (BET) [2], that amounted up to $800 \text{ m}^2/\text{g}$ for best materials.

In contrast to conventional carbon supported electrocatalysts, where catalytic particles of nm size are deposited onto the surface of onion-shaped carbon particles of several 10 nm diameter, the new catalyst type can be described consisting of in-situ formed graphite-like mesoscopic particles featuring a sponge-like matrix with cavities in the 10 nm range.

Studying the reduction current density at 0.7 V as a function of the electrical capacities of different electrodes, whose electrochemical active surface areas were varied, an exponent of 2.3 could be evaluated in a double logarithmic scale. Such a behaviour has not yet been observed on noble metal carbon supported catalysts. It points to the fact, that the efficiency of our catalysts is defined by the geometry of the carbon support (fractal structure) and the concentration and distribution of the catalytic centres integrated in the carbon matrix.

- [1] Hilgendorff, M.; Dorbandt, I.; Schulenburg, H.; Bron, M.; Fiechter, S.; Bogdanoff, P.; Tributsch, H.: *Platinfreies Chelat-Katalysator-material für die selektive Sauerstoffreduktion und Verfahren zu seiner Herstellung*. DE 101 32 490 A 1, Offenlegungstag 30.01.2003.
- [2] Bogdanoff, P.; Herrmann, I.; Hilgendorff, H.; Dorbandt, I.; Fiechter, S.; Tributsch, H.: *Journal of New Materials for Electrochemical Systems*, 2004 in press.
- [3] Bogdanoff, P.; Hilgendorff, M.; Schulenburg, H.; Fieber-Erdmann, M.; Dorbandt, I.; Tributsch, H.; Fiechter, S.: *World Renewable Energy Congress VII, Cologne, Proceedings, Schriften des Forschungszentrum Jülich, Vol. 26 (2003) 129-132 (D. Stolten and B. Edmonds (Eds.))*.
- [4] Schulenburg, H.: *Ruthenium- und eisenbasierte Katalysatoren für die elektrochemische Sauerstoffreduktion in Polymerelektrolytmembran-Brennstoffzellen*; PhD-Thesis, Freie Universität Berlin, 2002.

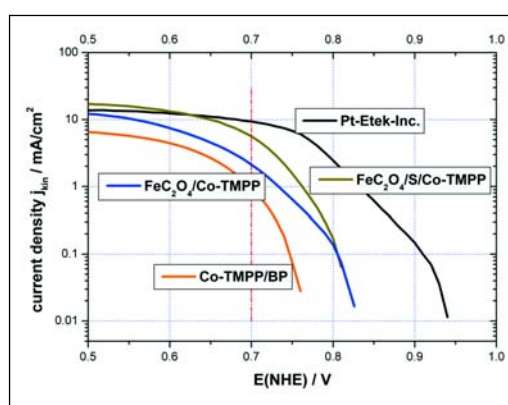


Fig. 2: Tafel-plots of differentially prepared iron-cobalt-catalysts.

Characterization and improvement of semiconductors and semiconductor junctions for solar energy conversion.

M. Kunst

■ HMI, SE5

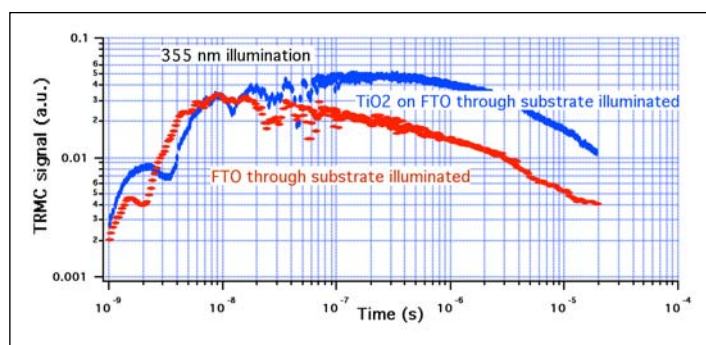


Fig. 1: TRMC signals induced by 355 nm light pulses (10 ns FWHM) in a FTO film on a glass substrate (red signal) and in $\text{TiO}_2/\text{FTO}/\text{glass}$ sample (blue signal).

Contactless and non invasive measurements of the transient photoconductance in the microwave frequency range (TRMC measurements) as developed in the HMI offer a versatile tool for the characterization of semiconductors and semiconductor junctions.

It was shown that the p a-Si:H/n c-Si heterojunction can be optimized by in-situ TRMC measurements: an unambiguous relation between the surface recombination velocity monitored (in-situ) during deposition of the interface and the efficiency of a solar cell based on the same interface was observed. Further, encouraging results were obtained in the characterization of TiO_2 powders for photocatalysis: relations between TRMC data and the efficiency of for a standard photocatalytic reaction were observed.

Here some exemplary TRMC results on transparent conductive oxides will be discussed in more detail.

Transparent conductive oxide (TCO)

In several newly developed solar cells, as for example the injection solar cell, an optically transparent contact is required. Based on the experiences with thin film solar cells conductive

oxides as highly doped ZnO and SnO are used. In the injection solar cell colloidal TiO_2 is deposited on F doped SnO (FTO) or In doped SnO (ITO) covered substrates. The theoretical description of the functioning of this solar cell considers the FTO (ITO) film as a metal serving as an ideal sink for electrons at the photo-active side of the device. This neglects the properties of these materials as (degenerate) semiconductors. TRMC measurements show that this is not warranted:

-Illumination of FTO films by 355 nm (super bandgap light) yields an appreciable photoconductance monitored by TRMC measurements (the red curve in Fig. 1) in spite of the low sensitivity of the TRMC technique for highly conductive samples. This signal is proportional to the excitation density. These observations point to the semiconductor character of the FTO-films.

Also TRMC measurements of colloidal TiO_2 films on FTO covered glass substrates are shown in Fig. 1. The sample is illuminated through the glass substrate, whereas the detecting microwaves are incident on the other (TiO_2) side. The initial signal is for both samples identical and consequently due to excess charge carriers (probably electrons) generated and mobile within the FTO film. However, in the $\text{TiO}_2/\text{FTO}/\text{glass}$ sample a slowly (compared to the optical generation of excess charge carriers finished in about 10 ns) rising additional component is observed from 10 ns–100 ns. The most plausible explanation of this slowly rising signal is injection of electrons generated in TiO_2 (where they do not contribute to the TRMC signal due to the low mobility) into the FTO part of the sample. In this case the risetime is intimately related to the diffusion time of electrons generated in TiO_2 to the TiO_2/FTO interface.

Consequently in the theoretical description of the injection solar cell the semiconductor character of the FTO-coated substrate must be taken into account and band bending at the TiO_2/FTO interface must be considered.

On the Problem of (Photo)-Degradation of Solid-State Nano-Composite Solar Cells

H. Tributsch
 ■ HMI, SE5

In recent years, nano-structured solid-state solar cells have attracted significant attention. As dye sensitization solar cells they were expected to overcome problems such as electrolyte degradation, confinement deficiencies, corrosion and photochemical deterioration encountered with cells including liquid electrolytes. In the case of organic composite solar cells, the significant progress seen for polymeric diodes should be transferred to solar cell technology. While many research groups have been competing for increasing solar cell efficiencies (4 % for solid-state dye solar cells [1], 3–4 % for organic solar cells [2], problems of long-term photostability have attracted very little attention. Research performed at the Hahn-Meitner Institute using photocurrent imaging techniques and selective illumination strategies showed that there is a problem and that it is quite dramatic. While state of the art organic solar cells, which are not protected against access of oxygen and humidity, are degrading within a few hours [3], solid-state dye solar cells degrade within a few days (100 hrs) to a fraction of their performance (20 %). While in the case of organic cells the inherent instability of the polymer (PPV) and of the fullerene are responsible, in the case of solid-state dye solar cells ($\text{TiO}_2/\text{dye}/\text{CuI}$) accumulation of electron capturing iodine and the break-up of the apparently essential hydrogen thiocyanate electron bridge were found to be responsible [4]. This experience suggests that competition for higher efficiencies of solid-state nano-composite solar cells only may not be economical for research in the

long-term. It is necessary to include phenomena, which are limiting cell stability. This will allow selection of useful components for cell develop-

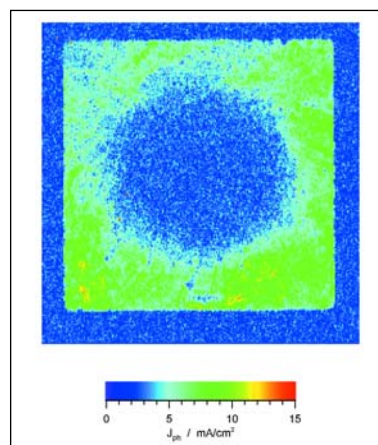


Fig. 1: A $\text{TiO}_2/\text{Ru-dye}/\text{CuI}$ solid-state solar cell, which at the beginning showed photocurrent densities in the red/yellow range, deteriorated to the above performance (1/3 of initial) within 75 hrs under simulated solar light illumination. While the round illumination spot is clearly visible, also the surrounding area has deteriorated. This indicates that migrating photogenerated carriers are also involved.

ment in an early stage of research. Research performed at the Hahn-Meitner Institute has shown that studies on photodegradation are especially useful in pinpointing specific mechanisms, which are essential for a long-term function of the cell. Typically those reaction steps start failing or degrading, which are critically involved in energy conversion. In this way mechanistic pathways can be identified, which also determine efficiency. The ultimate research aim should be to understand the mechanisms and to design nano-composite solar cells made-up of inherently stable components. The nano-materials involved have especially to satisfy the condition that quantum processes do not chemically modify or disrupt their interfaces, which mediate the reaction of photogenerated electrons of holes.

- [1] K. Tennakone, J. Bandara, K.P.M. Bandaranayake, G.R. A. Kumara, A. Konno, *Jpn. J. Appl. Phys.* **60**, 3558 (1986).
- [2] C.J. Brabec, N.S. Sariciftci, in *Conjugated Polymers*, Eds. G. Hadziannou, P. Van Hutten, Wiley-VCh, Weinigen (1999).
- [3] T. Jeranko, H. Tributsch, N.S. Sariciftci, J.C. Hummelen, *Sol. Energ. Mat. Sol. Cells*, in press (2004).
- [4] P.M. Sirimanne, H. Tributsch, *Sol. State Chem.*, in press (2004).

Successful Electrochemical Removal of Cu-S phases from CuInS₂ (CIS) Films

H. J. Lewerenz, B. Berenguier, M. Aggour, T. Wilhelm, H. Jungblut, M. Kanis

■ HMI, SE5

The application of the ternary chalcopyrite CuInS₂ on a large scale depends crucially on the omission of toxic steps and phases. One such step is the selective etching of Cu-S phases which are formed during CIS layer preparation. This is currently done with toxic KCN solutions. Previous experiments have shown that treatments of CIS in acidic vanadium(II/III) electrolytes yielded photoelectrochemical solar cells (PECS) of moderate efficiencies (1.3 %). The application of specific potential ramps as shown in Fig. 1 leads to a distinctly improved cell performance. At the start, the potential is increased from open circuit potential (−0.2 V) to 0.45 V, where the potential is kept constant for

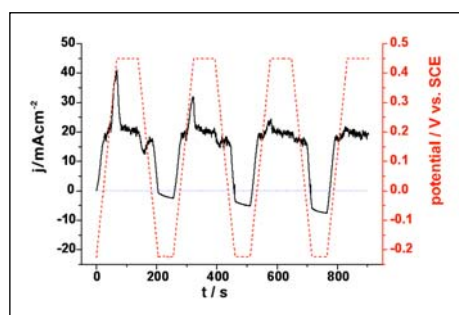


Fig. 1: Plots of current density (solid black line) and applied potential (dotted red line) vs. time during electrochemical etching in V²⁺/V³⁺ electrolyte (treatment A). At the end of each increasing potential ramp a current maximum caused by Cu_xS-dissolution is visible, which decreases with number of repetitions.

50 s (potentials are given vs. saturated calomel electrode, SCE). The current maximum indicates a dissolution reaction, the subsequent current drop a passivating behaviour. The potential is then reduced to −0.2 V and kept for another 50 s. With each repetition of this potential scan, the dissolution current peaks at the onset of the anodic potential plateaus become smaller. Concurrently, an increase of the cathodic photocurrents at the cathodic potential plateaus is observed. The procedure is continued until the dissolution peaks are no longer discernible and the photocurrents do not change any more (treatment A). The resulting films exhibit an efficiency of 2.8 % in PECS and 4 % in solid state solar cells (cf. Fig. 5, blue curve).

The investigation of correspondingly treated samples by X-ray emission spectroscopy (XES) indicates that Cu-S phases still remain which are identified as Cu₂S. From the standard Gibbs energies of formation for different Cu_xS species, the dissolution potential for Cu₂S can be expected to be more anodic than that for CuS [1]. A cyclic voltammogram of an as-grown CIS sample (see Fig. 2) clearly shows peaks attributable to different corrosion reactions. The dissolution of CIS itself starts at 0.6 – 0.8 V.

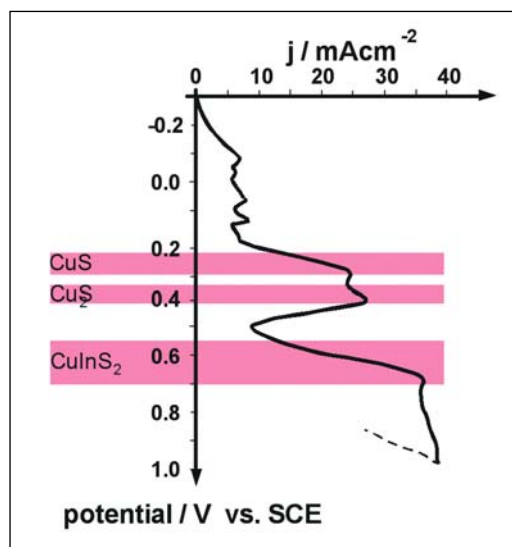


Fig. 2: First sweep of a cyclic voltammogram of a CIS film in V²⁺/V³⁺ electrolyte; estimated dissolution potential ranges for different species are marked red.

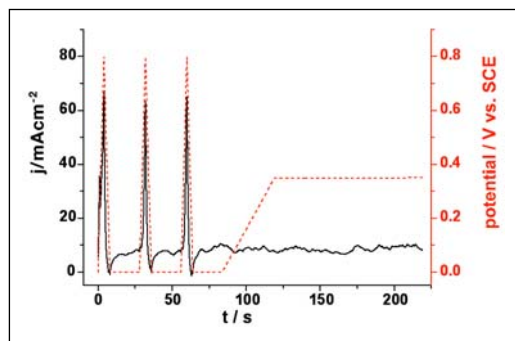


Fig. 3: Plots of current density (solid black line) and applied potential (dotted red line) vs. time during electrochemical etching in V^{2+}/V^{3+} electrolyte (treatment B). The dissolution potential sweeps were carried out with a scan speed of 50 mVs^{-1} , the last sweep was done using 10 mVs^{-1} .

Since the dissolution kinetics of Cu_2S are unknown, a short increase of the dissolution potential to 0.8 V is applied to dissolve the remaining Cu_2S and some CIS. These considerations lead to the electrochemical procedure shown in Fig. 3.

The potential is scanned between 0 V and 0.8 V and back to 0 V with a high scan rate (50 mVs^{-1}) to avoid undesired damage of the CIS substrate. Subsequently it is kept at 0 V for 50 s . This permits the removal of reaction products (and detached insoluble fragments) from the surface. The procedure is repeated for a few times (treatment B, see Fig. 3). This treatment leads, however, still to reduced solar conversion efficiencies of 1.1% (PECS) and 3% (solid state solar cells).

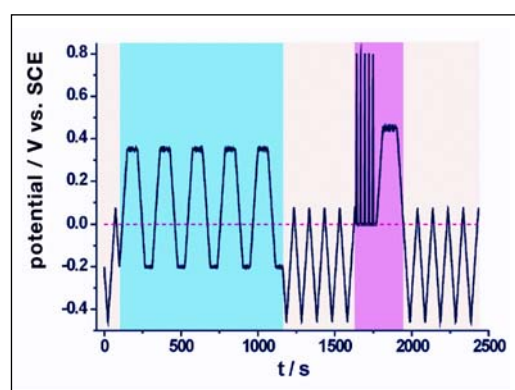


Fig. 4: Complete electrochemical potential vs. time characteristic consisting of treatment A (marked blue) and the more aggressive treatment B (marked pink). PECS evaluation steps are marked yellow.

The combination of both methods (treatment A and treatment B) leads finally to CIS layers with qualities comparable to those of KCN-etched specimen [2, 3]. Fig. 4 shows the complete potential program consisting of the modification procedures and inserted PECS testing steps which admit the in-situ control of the CIS film quality during the treatment.

Fig. 5 shows the j - V characteristic of a solid state solar cell made from a CIS sample after the combined electrochemical etching procedure (red curve). The respective characteristics are: $\eta = 8 \%$, $ff = 52 \%$, $V_{oc} = 0.69 \text{ V}$ and $j_{sc} = 10.5 \text{ mAcm}^{-2}$. For a KCN etched reference sample $\eta = 11.2 \%$, $ff = 69.4 \%$, $V_{oc} = 0.72 \text{ V}$, $j_{sc} = 11 \text{ mAcm}^{-2}$ are obtained.

The results show that a directed electrochemical removal of deleterious Cu-S phases from CIS layers is possible without the use of cyanide solutions. Further improvements, particularly with respect to a simplification of the procedure are currently under investigation.

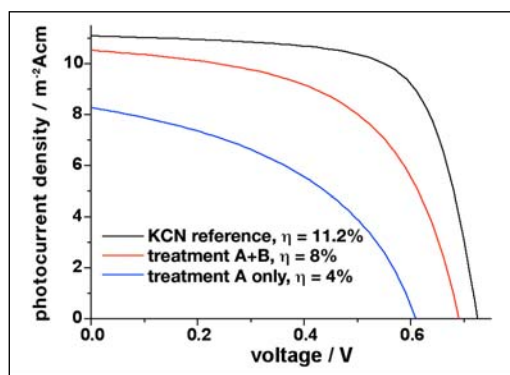


Fig. 5: Solid state solar cell characteristics of CIS layers after treatment A (blue), after combined treatment A and B (red) and after KCN-etch as reference (black). The measurements were made using an AM 1.5 sun simulator.

- [1] D. Cahen, Y. Mirovsky, J. Phys. Chem. **89**, 2818 (1985).
- [2] B. Berenguier, H.J. Lewerenz, patent applied for (AZ:103 44 315.0)
- [3] B. Berenguier, H. J. Lewerenz, J. Electrochem. Soc. Lett., submitted.